

JGR Solid Earth

RESEARCH ARTICLE

10.1029/2023JB026816

Difference in Relative Paleointensity Recording Efficiency of Magnetic Mineral Constituents in a Sediment Core Off Chile

Toshitsugu Yamazaki¹ , Jiayi Li¹ , Takaya Shimono^{1,2,3}, and Toshiya Kanamatsu⁴ 

¹Atmosphere and Ocean Research Institute, The University of Tokyo, Kashiwa, Japan, ²Graduate School of Life and Environmental Sciences, University of Tsukuba, Tsukuba, Japan, ³Kaiyo Engineering CO., LTD., Tokyo, Japan, ⁴Subduction Dynamics Research Center, Research Institute for Marine Geodynamics, Japan Agency for Marine-Earth Science and Technology, Yokosuka, Japan

Key Points:

- Magnetofossil and detrital partially oxidized unprotected magnetite are the major constituents of magnetic mineral assemblage
- Little overlap in coercivity distribution of the two components enabled separate evaluation of relative paleointensity (RPI) recording efficiency
- RPI recording efficiency of magnetofossil is lower than that of detrital unprotected magnetite/maghemite

Supporting Information:

Supporting Information may be found in the online version of this article.

Correspondence to:

T. Yamazaki,
yamazaki@aori.u-tokyo.ac.jp

Citation:

Yamazaki, T., Li, J., Shimono, T., & Kanamatsu, T. (2023). Difference in relative paleointensity recording efficiency of magnetic mineral constituents in a sediment core off Chile. *Journal of Geophysical Research: Solid Earth*, 128, e2023JB026816. <https://doi.org/10.1029/2023JB026816>

Received 28 MAR 2023

Accepted 10 AUG 2023

Author Contributions:

Conceptualization: Toshitsugu

Yamazaki, Toshiya Kanamatsu

Data curation: Toshitsugu Yamazaki

Formal analysis: Toshitsugu Yamazaki, Jiayi Li

Funding acquisition: Toshitsugu

Yamazaki, Toshiya Kanamatsu

Investigation: Toshitsugu Yamazaki,

Jiayi Li, Takaya Shimono, Toshiya Kanamatsu

Writing – original draft: Toshitsugu Yamazaki

Abstract Progress of relative paleointensity (RPI) estimations using marine sediments has greatly contributed to better understanding of the behavior of the past geomagnetic field. To enhance further the reliability of RPI estimations, we must overcome the problem that climatically induced variations of magnetic-mineral assemblages in sediments may influence RPI records. Two major constituents of magnetic-mineral assemblages in marine sediments are magnetofossils and detrital magnetic minerals, and the latter consists of silicate-hosted magnetic inclusions and unprotected magnetic minerals. It is necessary to understand different RPI recording efficiencies among those constituents to tackle the problem, but previous evaluations were inconclusive. We studied this issue using a sediment core taken from the southeast Pacific Ocean. Rock-magnetic investigations revealed that the magnetic mineral assemblage of this core during the last ~900 Kyr is a mixture of low-coercivity magnetofossils and middle-coercivity detrital unprotected partially oxidized magnetite. Natural remanent magnetization versus isothermal remanent magnetization demagnetization diagram showed strong convex curvature, and RPI signals carried by the two components could be separated by calculating RPI from the gradients of 20–40 and 70–160 mT segments. We confirmed that RPI recording efficiency of magnetofossils is lower than that of detrital unprotected magnetites/maghemites. Because of the marginal overlap between the coercivity ranges of the two components, changes in their relative abundance do not influence RPI estimations. This condition is ideal for RPI estimations, and the resulted RPI curve closely coincides with that of the PISO-1500 stack despite changes in the relative abundance of the two components.

Plain Language Summary Marine sediments potentially preserve records of geomagnetic field intensity variations in the past (paleointensity), which may be important for life on the Earth to shield influx of high-energy particles from the universe. A serious problem recognized by previous studies is that paleointensity records from sediments sometimes include artificial changes induced by sediment lithology changes reflecting varying depositional environments. Two major constituents of magnetic minerals in sediments, which records paleointensity variations, are magnetites produced by magnetotactic bacteria, called magnetofossils, and inorganic magnetic minerals originated from weathering of rocks on land or materials of volcanic eruptions. Our study using a sediment core taken from the southeast Pacific Ocean revealed that magnetofossils yield lower paleointensity values than inorganic magnetic minerals. This implies that temporal changes in the relative abundance of magnetofossils and inorganic magnetic minerals in sediments may cause the artificial paleointensity variations. We could obtain a reliable paleointensity record from the studied sediments by evaluating separately the magnetizations carried by the two magnetic-mineral components, which utilized the observations that the two magnetic-mineral components have different resistance to an external magnetic field.

1. Introduction

Progress of relative paleointensity (RPI) estimations using marine sediments have greatly contributed to better understanding of the behavior of the geomagnetic field in the past and relating dynamics of the Earth's core. Examples of the achievement of RPI estimations are the establishment of the global RPI stacks such as the Sint-2000 stack for the last 2 Myr (Valet et al., 2005) and the PISO-1500 stack for the last 1.5 Myr (Channell et al., 2009). For older ages, global RPI stacks have not yet been established, but the number of RPI curves reported is increasing (Ohneiser et al., 2013; Tauxe & Hartl, 1997; Yamamoto et al., 2014, 2022; Yamazaki & Yamamoto, 2018). On the other hand, limitations of the current RPI estimations are widely recognized. A

© 2023 The Authors.

This is an open access article under the terms of the [Creative Commons Attribution-NonCommercial License](https://creativecommons.org/licenses/by-nc/4.0/), which permits use, distribution and reproduction in any medium, provided the original work is properly cited and is not used for commercial purposes.

Writing – review & editing: Jiayi Li,
Takaya Shimono, Toshiya Kanamatsu

significant problem is that climatically induced variations of magnetic-mineral assemblages in sediments may influence RPI records, in what is known as climatic contamination (Valet et al., 2011; Xuan & Channell, 2008; Yamazaki et al., 2013). For enhancing reliability of RPI estimations, this problem needs to be understood thoroughly, and then a solution should be devised.

Two major constituents of magnetic-mineral assemblages in marine sediments are magnetofossils and detrital magnetic minerals (e.g., Channell et al., 2013; Chen et al., 2017; Roberts et al., 2012; Yamazaki, 2008). It is considered that different RPI recording efficiency between these two components may be responsible for the climatic contamination, which is likely originated from their different acquisition efficiencies of natural remanent magnetization (NRM) and the normalizers usually used for RPI estimations, namely the anhysteretic remanent magnetization (ARM) and the isothermal remanent magnetization (IRM). Some previous studies using Pacific marine sediments proposed that RPI recording efficiency of the magnetofossil component is lower than that of the detrital component, and that increasing proportion of the magnetofossil component causes underestimation of RPI (Gai et al., 2021; Inoue et al., 2021; Li et al., 2022). This explains frequently reported anti-correlation between RPI and the ratio of ARM susceptibility to saturation IRM ($k_{\text{ARM}}/\text{SIRM}$) (Hofmann & Fabian, 2009; Inoue et al., 2021; Li et al., 2022; Sakuramoto et al., 2017; Yamazaki et al., 2013), as $k_{\text{ARM}}/\text{SIRM}$ is a proxy for the proportion of the magnetofossil to detrital components (Egli, 2004; Yamazaki, 2008; Zhang et al., 2022) as well as magnetic grain size (Banerjee et al., 1981; King et al., 1982). The conclusion of lower RPI recording efficiency for magnetofossil by Li et al. (2022) is derived from the observations that RPI calculated from a higher-coercivity fraction is smaller than that from a lower-coercivity fraction and that the higher-coercivity fraction in their studied sediments is mainly carried by magnetofossil whereas the proportion of the detrital component is larger in the low-coercivity fraction. The opposite conclusion was, however, obtained from some sediment cores using a similar method (Chen et al., 2017; Ouyang et al., 2014). Also in these studies, a higher-coercivity fraction (50–80 mT) is considered to be carried mainly by magnetofossil.

Recently, the important role of silicate-hosted magnetic inclusions as a carrier of remanent magnetization in marine sediments has become recognized (Chang et al., 2016, 2021; Chen et al., 2017; Zhang et al., 2018). However, their efficiency in acquiring a detrital remanent magnetization (DRM) is not well understood. The DRM acquisition efficiency may be controlled by various factors, including the total magnetic moment of the host silicate crystals and their grain sizes, and the domain state of magnetic inclusions. Because of the lower ratio of magnetic moment to volume of silicate crystals with magnetic inclusions, their RPI recording efficiency is expected to be lower than that of unprotected magnetic grains. Accordingly, RPI contributions from these two classes of detrital magnetic minerals need to be evaluated separately. The detrital component of the sediments studied by Li et al. (2022) is dominated by unprotected magnetites whereas that of Chen et al. (2017) would mainly be silicate-hosted magnetic inclusions. This may have led the opposite conclusion regarding RPI recording efficiency of magnetofossil (Li et al., 2022).

Magnetic mineral compositions of sediments vary from place to place depending on depositional environments. Hence, we need to expand the research to global sediments in order to understand comprehensively the differences of RPI recording efficiency among constituents of magnetic mineral assemblages. Here we have conducted a paleo- and rock magnetic study of a sediment core taken from the southeast Pacific Ocean. Sediments of this region were less studied paleomagnetically so far. We will show that RPI recording efficiency of magnetofossils is lower than detrital partially oxidized unprotected magnetites.

2. Samples

A piston core MR0806-PC3 of approximately 19.66 m in length was taken from the southeast Pacific Ocean off Chile during the *R/V Mirai* MR08-06 cruise in 2009 (Abe, 2009) (Figure 1). The position of the coring site is 48°24.95'S, 80°28.43'W, and the water depth is 4,049 m. The site is to the southwest of the Chile Triple Junction, and the age of the seafloor at the site is about 15 Ma. The core consists of silty clay, diatomaceous silty clay, and calcareous silty clay. The sediments are lightly to heavily mottled and bioturbated. The bottom 0.59 m of the core was excluded from this study because of flow-in.

Core color reflectance was measured onboard at 1 cm intervals on split half-core surfaces through transparent polyethylene wrap with a Minolta CM-2002 reflectance photospectrometer using 400–700 nm in wavelengths. To quantify the color reflectance, the $L^*a^*b^*$ system is used in this study. The color of the core is light gray

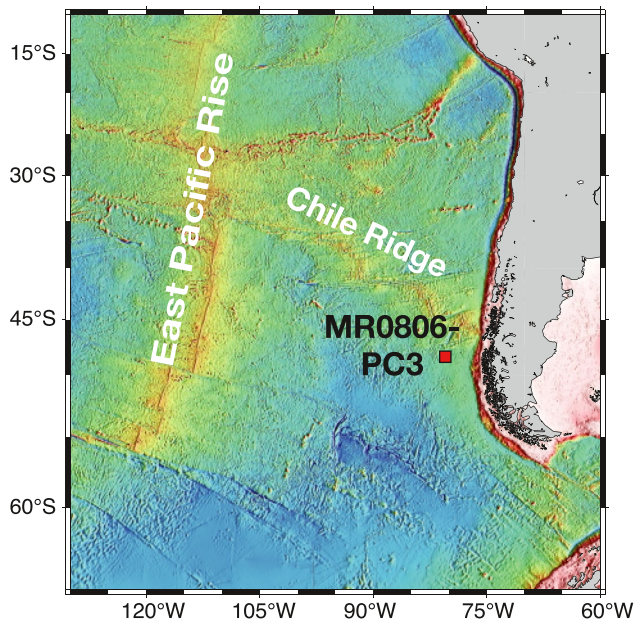


Figure 1. Map showing the location of Core MR0806-PC3 and bathymetry in the southeast Pacific Ocean.

to grayish olive, and more grayish in the deeper part of the core in general (Figure S1 in Supporting Information S1). Cyclic color changes are remarkable, in particular in the deeper part of the core.

Discrete samples for paleo- and rock-magnetic measurements were taken continuously onboard from half-split core surfaces using 7 cm³ plastic cubes. In total 487 discrete samples were obtained. The samples were tightly sealed to prevent dehydration before measurements.

3. Natural Remanent Magnetization

NRM of every other sample, about 5 cm intervals in the core, was measured using a pass-through cryogenic magnetometer (2G Enterprises model 760R) at Marine Core Research Institute (MaCRI), Kochi University. Stepwise alternating-field (AF) demagnetization was conducted at 10 or 11 steps up to a peak AF field of 80 mT using an in-line AF demagnetizer of the pass-through magnetometer system. It was revealed that a significant portion of the NRM, about 30%–45% of the initial intensity, remains after AF demagnetization at 80 mT (Figure 2). The presence of large contributions with >80 mT coercivities is unusual for deep-sea sediments (e.g., Heller et al., 1984; Opdyke et al., 1966; Yamazaki & Ioka, 1994; Yamazaki & Yamamoto, 2018).

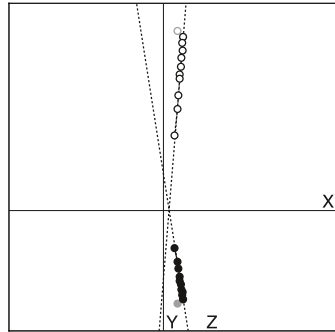
Then, in order to further demagnetize the NRM, 72 discrete samples were AF demagnetized at 16 steps up to 160 mT and measured using a fully automated spinner magnetometer with a build-in tumbling AF demagnetizer (Natsuhara-Giken D-spin) at Atmosphere and Ocean Research Institute (AORI), The University of Tokyo. Another eight samples were demagnetized at 14 steps up to 140 mT with a standalone tumbling AF demagnetizer (Natsuhara-Giken DEM-95) and measured with a cryogenic magnetometer for discrete samples (2G Enterprises model 755) at MaCRI, Kochi University. Ninety-five percent or more of initial NRM were demagnetized at 140 or 160 mT (Figure 3). The samples demagnetized up to 140 or 160 mT were taken at about 24 cm intervals. Remaining NRM intensities after 80 mT AF demagnetization using the tumbling AF demagnetizers of the D-spin or DEM-95 are about 30% smaller than those using the static demagnetizer of the pass-through magnetometer system. This is due to the higher demagnetization efficiency of the tumbling method with respect to the static AF demagnetizer, due to the exposure of all minerals to the AF field along directions of minimum coercivity.

Characteristic remanent magnetization (ChRM) direction was determined using principal component analysis (Kirschvink, 1980; Figures 2 and 3). The demagnetization interval with the smallest maximum angular deviation (MAD) was adopted. The fitting was not anchored to the origin, but the deviation from the origin was very small. A secondary component of probably viscous remanent magnetization origin was removed at first few AF steps, and ChRM direction is well resolved (Figures 2 and 3). Most samples have MAD of less than 10° except for near polarity transitions (Figure 4). There is no systematic difference in ChRM directions between the results of AF demagnetization up to 80 mT measured with the pass-through magnetometer and those of up to 160 mT measured with the spinner magnetometer (Figure 4), although the scatter in the directions and MAD values of the latter are larger due to lower sensitivity of the spinner magnetometer than the pass-through cryogenic magnetometer.

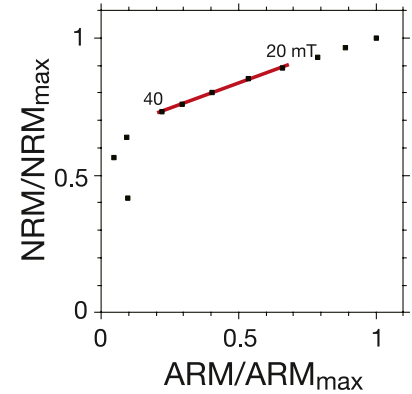
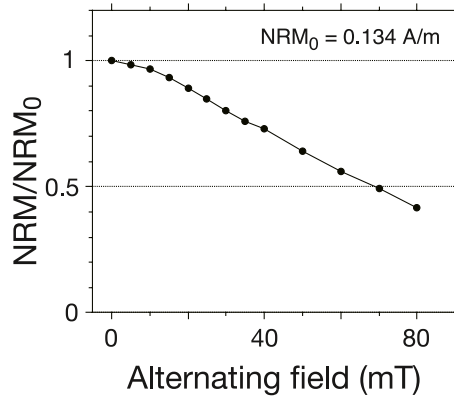
From the NRM declination and inclination, it is concluded that the Matuyama-Brunhes polarity transition occurs at approximately 11.5 m in depth (Figure 4). A short normal-polarity interval at ~17.0 m in depth is considered to be a manifestation of the Cobb Mountain subchron (1.180–1.215 Ma according to Gradstein et al. (2020)). The age of the bottom of the core is estimated to be approximately 1.36 Ma, and the average sedimentation rate is 13.9 m/Myr.

The average inclinations of the samples measured with the pass-through cryogenic magnetometer system are $-64.4^\circ \pm 4.5^\circ$ during the Brunhes chron and $63.9^\circ \pm 6.5^\circ$ during the Matuyama chron excluding the Jaramillo and Cobb Mountain subchrons. The mean inclination anomaly calculated as the deviation of the observed inclination from the inclination expected from the geocentric axial dipole field at the site latitude ($\pm 66.1^\circ$) is 1.7° and -2.2° for the Brunhes and Matuyama chrons, respectively. According to the time-averaged field models for the last 5 Myr (Johnson & Constable, 1997) and for the last 10 Myr (Cromwell et al., 2018), the inclination anomaly is negative during the normal polarity and positive during the reversed polarity in general, and larger in magnitude

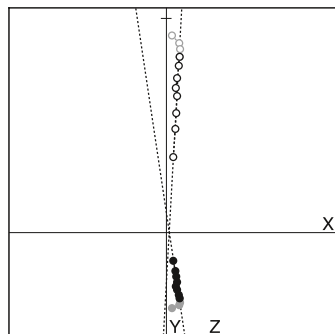
No. 789 (2.65m)



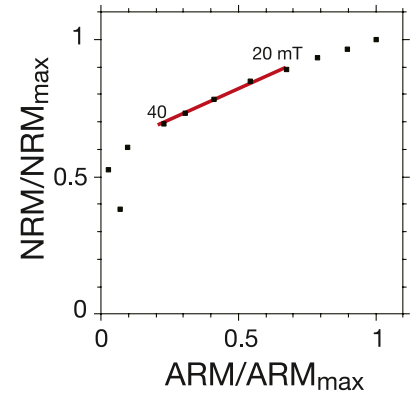
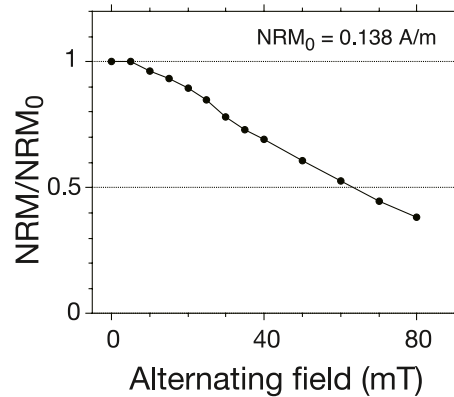
PCA: MAD=1.3, N=10 (10.0–80.0mT)
D=81.0, I=-62.3



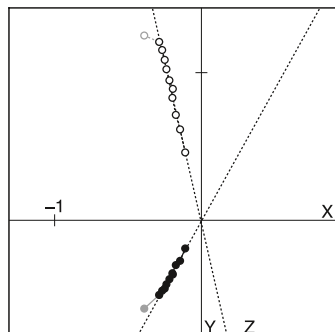
No. 911 (5.50m)



PCA: MAD=1.4, N=8 (20.0–80.0mT)
D=81.5, I=-69.1



No. 1123 (10.42m)



PCA: MAD=1.8, N=10 (10.0–80.0mT)
D=119.2, I=-64.9

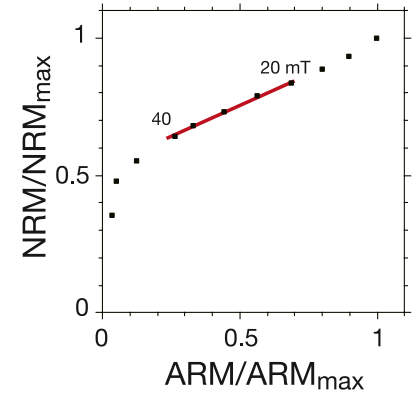
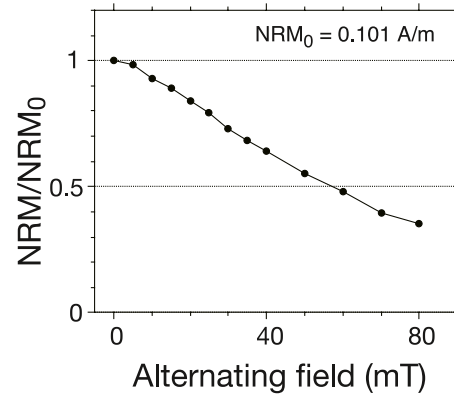


Figure 2. Examples of natural remanent magnetization (NRM) and relative paleointensity (RPI) estimation normalized by anhysteretic remanent magnetization (ARM) for samples measured with the pass-through cryogenic magnetometer system. Left panels show stepwise alternating-field (AF) demagnetization of NRM. Open (solid) circles are the projection of vector end points on the vertical (horizontal) plane. The core is not azimuthally oriented. Black dashed line indicates characteristic remanent magnetization (ChRM) direction, and data points of gray circles were not used to calculate the ChRM. Middle panels show decay of NRM intensity during stepwise AF demagnetization. Right panels show RPI estimation from a best-fitting slope (red line) on a diagram plotting a pair of NRM and ARM for each AF demagnetization step. A coercivity interval from 20 to 40 mT was used for RPI estimation normalized by ARM.

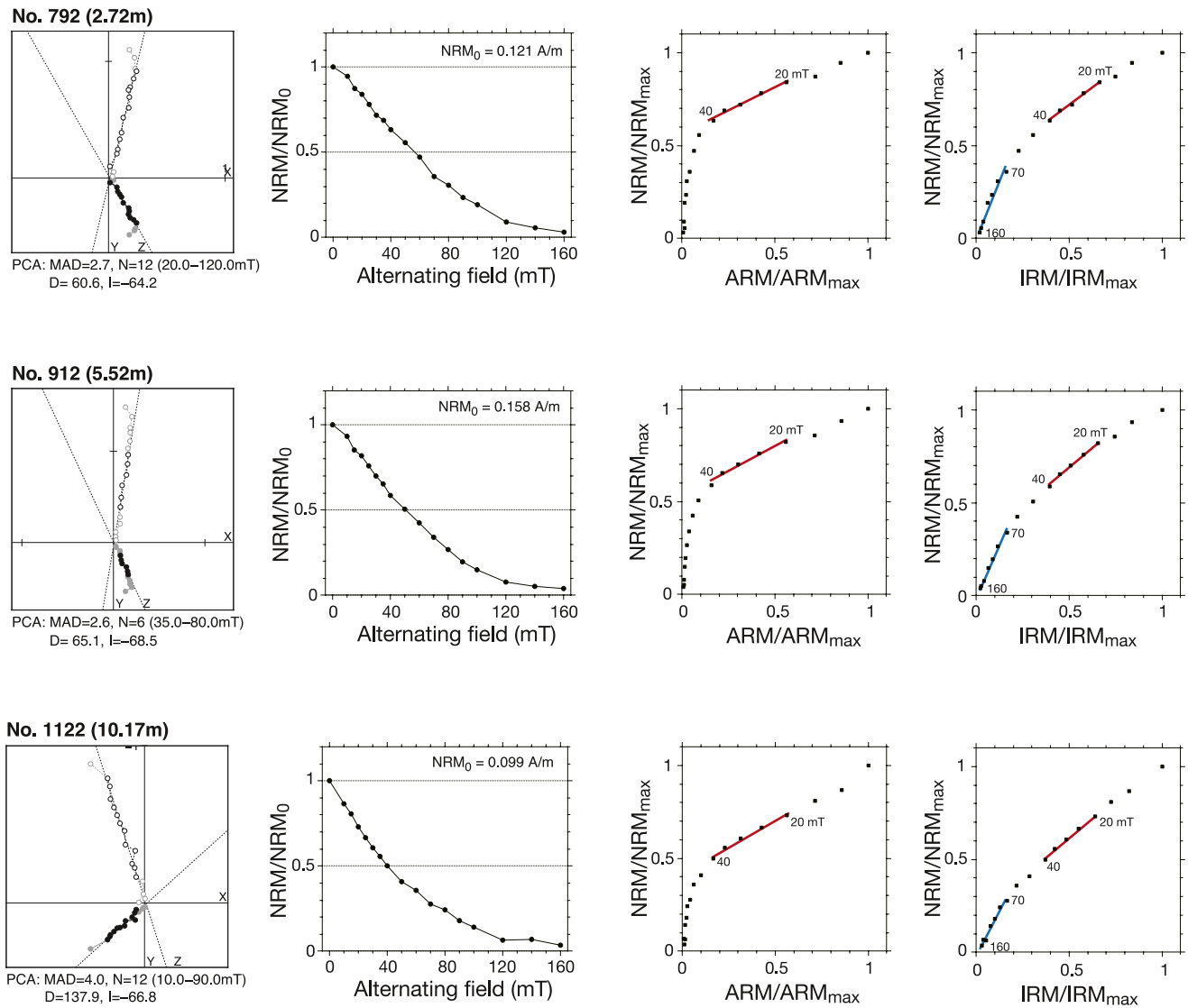


Figure 3. Examples of natural remanent magnetization (NRM) and relative paleointensity (RPI) estimation normalized by anhysteretic remanent magnetization (ARM) and isothermal remanent magnetization (IRM) for samples measured with the automated spinner magnetometer system. Leftmost panels shows stepwise alternating-field (AF) demagnetization of NRM. Open (solid) circles are the projection of vector end points on the vertical (horizontal) plane. The core is not azimuthally oriented. Black dashed line indicates characteristic remanent magnetization (ChRM) direction, and data points of gray circles were not used to calculate the ChRM. The second row from the left shows decay of NRM intensity during stepwise AF demagnetization. The third row from the left shows RPI estimation from a best-fitting slope (red line) on NRM-ARM demagnetization diagram. A coercivity interval between 20 and 40 mT was used for RPI estimation normalized by ARM. Rightmost row shows RPI estimation from a best-fitting slope on a NRM-IRM demagnetization diagram. Coercivity intervals from 20 to 40 mT (red) and from 70 to 160 mT (blue) were adopted for RPI estimation normalized by IRM.

at low latitudes. The southeast Pacific represents an exception, with slightly positive (negative) inclination anomalies during the normal (reversed) polarity. The result of this core is consistent with these models.

4. Rock Magnetism

4.1. Methods

4.1.1. Bulk Magnetic Properties

Magnetic susceptibility was measured using a KappaBridge MFK2-FA susceptometer at AORI, The University of Tokyo. ARM was imparted at a peak AF of 80 mT superimposed on a DC field of 0.1 mT and measured with the pass-through magnetometer system for samples that were AF demagnetized by this magnetometer system. For the samples that were AF demagnetized by the tumbling demagnetizers, ARM was imparted at a peak AF field

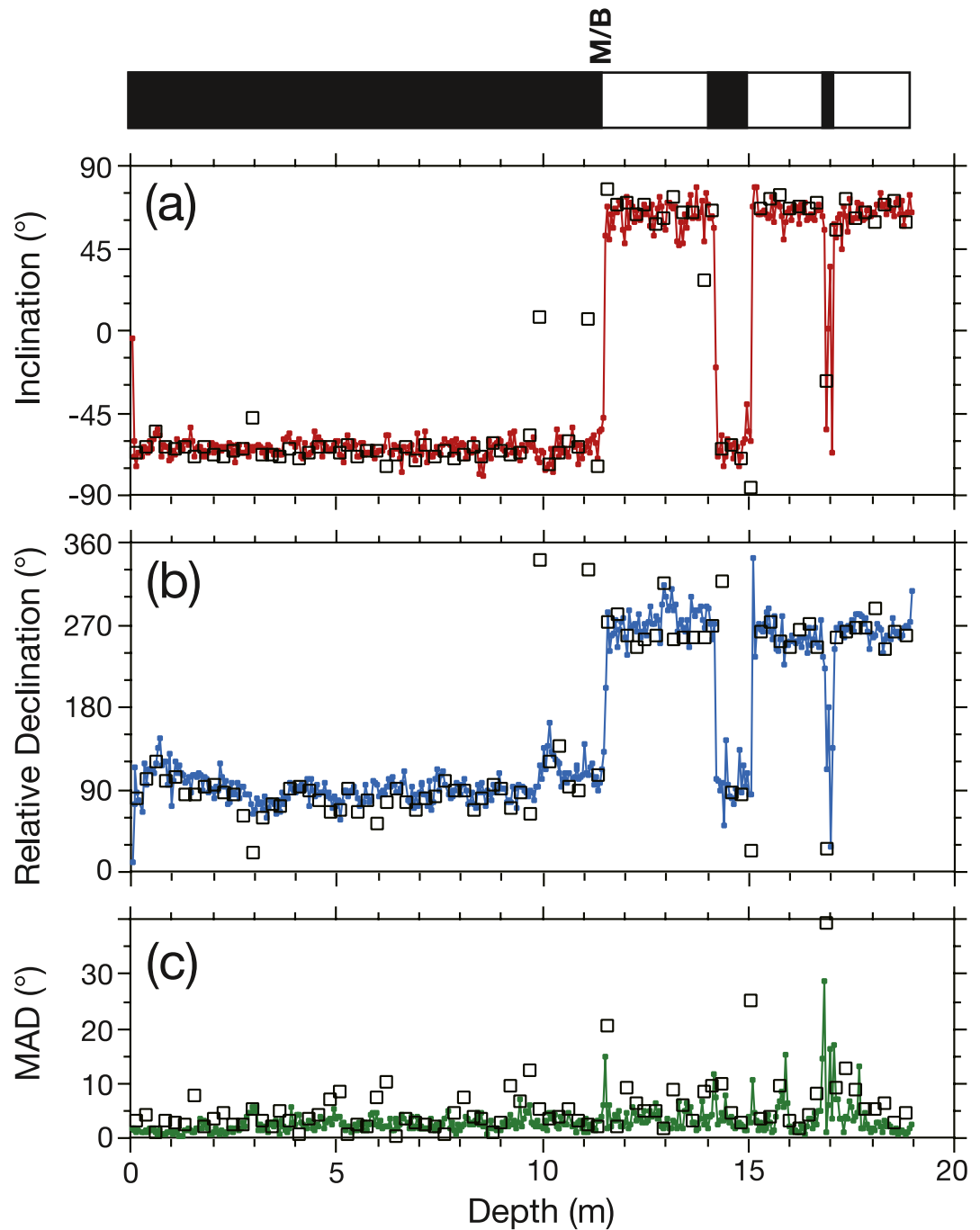


Figure 4. Downcore variations of characteristic remanent magnetization directions: (a) inclination, (b) relative declination, and (c) maximum angular deviation. Colored data points connected with lines were measured using the pass-through cryogenic magnetometer, and open squares were measured with the automated spinner magnetometer. Magnetic polarity interpretation is shown on the top.

of 160 mT superimposed on a DC field of 0.05 or 0.1 mT and measured with the automated spinner magnetometer system. Differences in AF frequency and decay time between the two systems may cause different ARM acquisition efficiency, and hence only ARMs imparted with the pass-through magnetometer system were used for rock-magnetic discussion in this chapter. ARMs imparted with the spinner magnetometer system will be used later for RPI estimations. IRM was given by a pulse magnetizer (ASC IM-10-30) at AORI, The University of Tokyo, and measured using the spinner magnetometer. First, IRM was imparted at 2.5 T, which is regarded as

SIRM in this paper. Then, IRMs of 0.1 and 0.3 T were successively imparted in the direction opposite to the initial IRM. S ratios ($S_{-0.1T}$ and $S_{-0.3T}$) were calculated according to the definition of Bloemendal et al. (1992).

4.1.2. Low-Temperature Measurements

Low-temperature magnetic measurements were conducted on 10 selected samples using a low-temperature superconducting quantum interference device (SQUID) susceptometer (Quantum Design MPMS-XL5) at MaCRI, Kochi University. The main purpose of the measurements was to obtain information on magnetic mineralogy, in particular for estimating oxidation state of magnetite (Özdemir & Dunlop, 2010). Hence the samples for the measurement were selected to cover variations in S -ratios and color reflectance. First, an IRM was imparted at 300 K in a 3 T field, and magnetization changes were measured at approximately 2 K intervals during cycling the temperature between 300 and 10 K in a nearly zero field. Then, the samples were cooled from 300 to 10 K in a 3 T field, which was followed by measurement of the IRM up to 300 K at approximately 2 K intervals.

4.1.3. First-Order Reversal Curve (FORC) Measurements

First-Order Reversal Curve (FORC) diagram provides information on the distribution of coercivity (H_c) and local interaction field (H_u) of a magnetic particle assemblage (Pike et al., 1999; Roberts et al., 2000), and has become widely used to quantitatively characterize magnetic mineral assemblages in rock- and environmental magnetic studies (Egli, 2021; Roberts et al., 2014, 2022). FORC measurements were conducted on 22 samples using an alternating-gradient magnetometer (AGM, Princeton Measurements Corporation MicroMag 2900) at AORI, The University of Tokyo. The samples were selected to cover variations in $k_{ARM}/SIRM$. A total of 133 FORCs were measured for each sample, with H_c between 0 and 140 mT, H_u between -50 and 50 mT, and field spacing of approximately 2 mT. For 4 out of 22 samples, H_u ranged from 0 to 100 mT, and the number of FORCs was 113. The maximum applied field was 1.0 T, and the averaging time for each measurement point was 400 ms. FORCinel software (Harrison & Feinberg, 2008, version 3.06 in 2022) was used to produce FORC diagrams, and the VARIFORC algorithm of Egli (2013) was used to smooth the data with smoothing parameters of $S_{c0} = 4$, $S_{b0} = 3$, and $S_{c1} = S_{b1} = 7$. When resulted in low signal-to-noise ratios, the measurements were repeated three times and the data were stacked.

4.1.4. IRM Component Analysis

IRM acquisition curves were measured using the AGM to estimate magnetic mineral composition from coercivity distribution. The experiment was conducted on the same samples for the FORC measurements. One hundred measurements were made at field steps ranging from 3 mT to 1.0 T. The IRM acquisition curves were decomposed into magnetic coercivity components using the method of Kruiver et al. (2001) assuming that IRM acquisition curves are a linear addition of components represented by cumulative log-Gaussian functions.

4.1.5. Transmission Electron Microscopy (TEM)

TEM observation of magnetic extracts was conducted to directly observe magnetic minerals, in particular to identify magnetofossils from their characteristic morphology and grain size confined within the single-domain (SD) range (e.g., Kopp & Kirschvink, 2008). Two representative samples with high and average $k_{ARM}/SIRM$ values, at 6.06 and 6.94 m in depth, were selected for the observation. Magnetic minerals were extracted using a magnetic finger (Kirschvink et al., 1992). The extraction procedure and TEM grid preparations are described in Yamazaki and Shimono (2013). A TEM (JEOL JEM-1400) at AORI, The University of Tokyo, operated at 120 kV, was used for the observation.

4.1.6. Magnetization Carried by Silicate-Hosted Magnetic Inclusions

In order to estimate the contribution of silicate-hosted magnetic inclusions to the magnetization of the sediments, quartz and feldspar were extracted with sodium pyrosulfate ($Na_2S_2O_7$) fusion technique (Blatt et al., 1982; Clayton et al., 1972; Stevens, 1991; Syers et al., 1968). For detailed procedures, refer Usui et al. (2018) and Li et al. (2022). Three samples at 1.88, 6.06, and 11.91 m in depth were subjected to the chemical digestion. The fraction of magnetization carried by silicate-hosted magnetic inclusions was estimated from difference in SIRM between untreated sediments and residues of the chemical digestion.

4.2. Results and Interpretation

Magnetic susceptibility fluctuates around 5×10^{-4} SI except for a few spikes and a conspicuous low at ~ 6 m in depth (Figure 5a). $k_{ARM}/SIRM$ shows a long-term upcore decreasing trend above ~ 13 m in depth (Figure 5b),

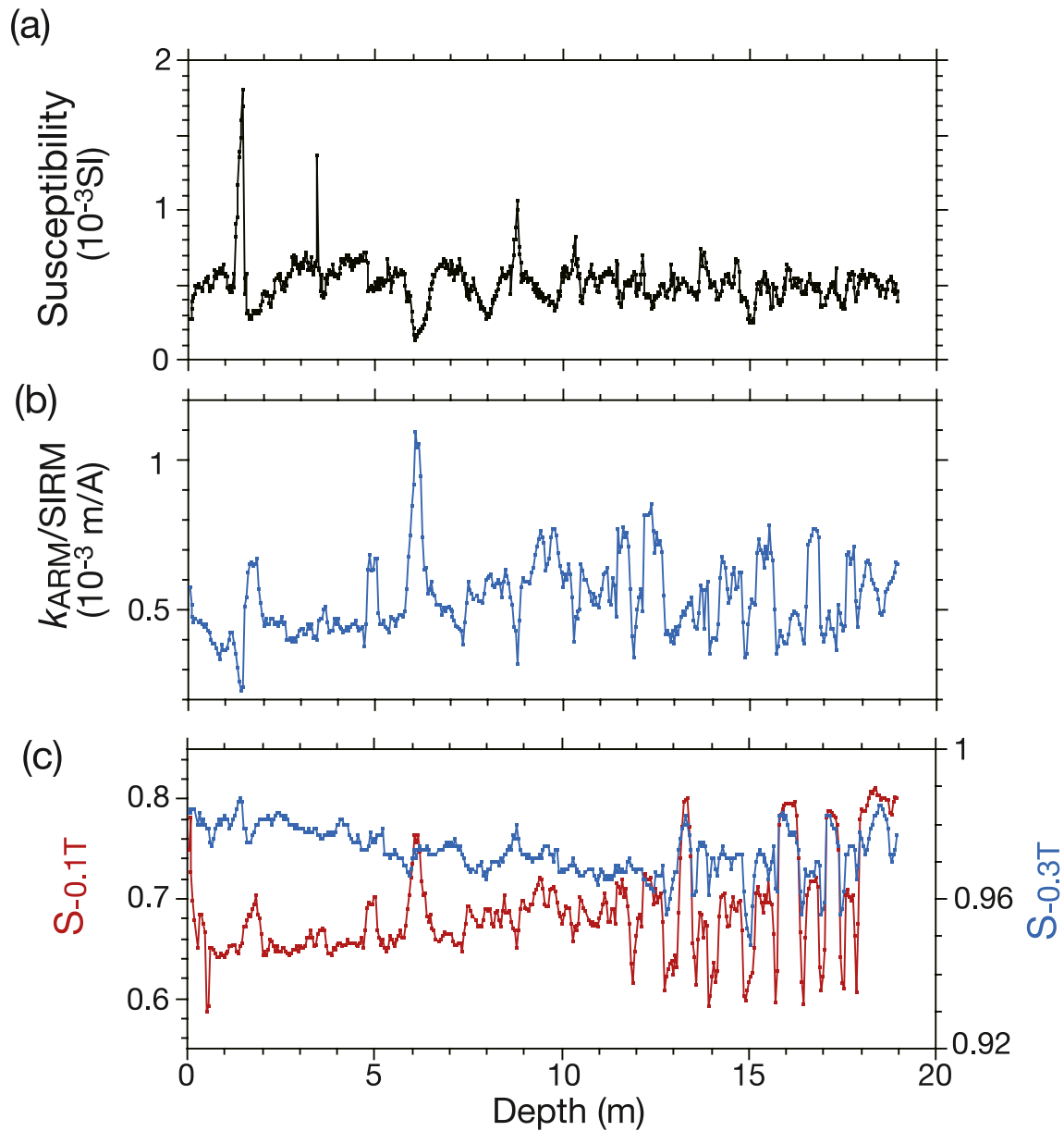


Figure 5. Downcore variations of bulk magnetic properties: (a) magnetic susceptibility, (b) the ratio of anhysteretic remanent magnetization susceptibility (k_{ARM}) to saturation isothermal remanent magnetization, and (c) S -ratio: $S_{-0.1T}$ (red) and $S_{-0.3T}$ (blue).

suggesting a decreasing proportion of magnetofossils to detrital magnetic grains. $S_{-0.1T}$ also shows an upcore decreasing trend above ~ 13 m (Figure 5c). A magnetic susceptibility low at ~ 6 m coincides with a high in $k_{ARM}/SIRM$ and $S_{-0.1T}$. Below ~ 13 m, $S_{-0.1T}$ shows large fluctuations, suggesting significant changes in magnetic mineral composition of the sediments.

IRM component analyses revealed that IRM of all samples is carried mainly by two magnetic components: low- and middle-coercivity components (Figures 6a–6d; Figures S2a–S2j in Supporting Information S1). The low-coercivity component has the mean coercivity of approximately 40 mT and dispersion parameter (DP) of 0.22 throughout the core. The mean coercivity and DP of the middle-coercivity component are 110–120 mT and 0.20–0.22, respectively, for the samples above 13 m in depth, whereas samples from the deeper part of the core at 13.35 and 16.05 m have significantly lower mean coercivity of ~ 75 mT (Figure 6d; Figures S2h and S3 in Supporting Information S1). This is consistent with higher $S_{-0.1T}$ of these samples (Figure 5c). The occurrence of a middle-coercivity component with the mean of ~ 100 mT was often reported from Pacific marine sediments

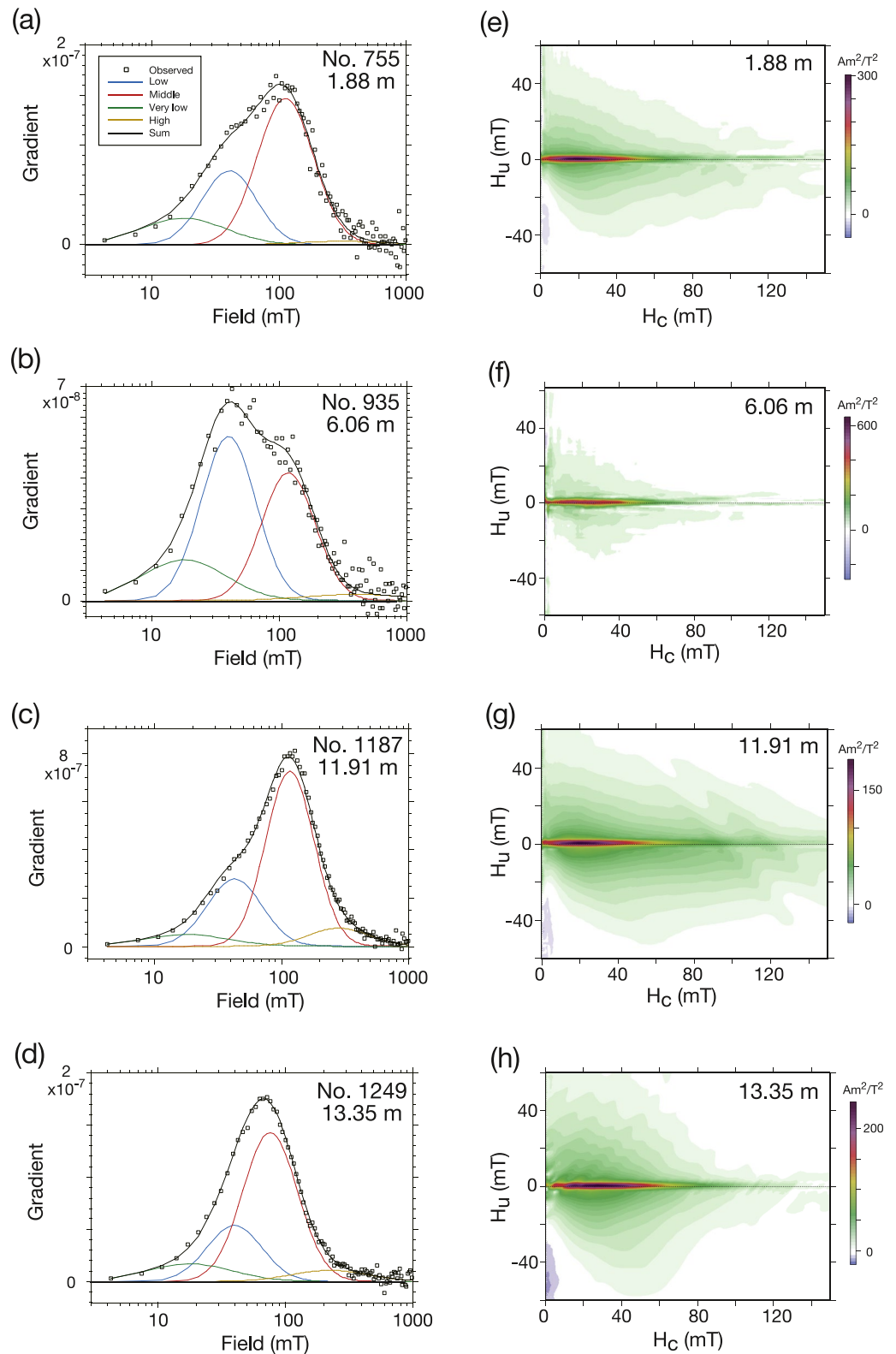


Figure 6. (a–c) Examples of isothermal remanent magnetization (IRM) component analyses. Squares represent data points that define the gradient of IRM acquisition curves, which can be described by the sum (black curve) of two dominant components, low-coercivity (blue) and middle-coercivity (red) components, and other two minor components, very-low-coercivity (green) and high-coercivity (orange) components. (d–f) Corresponding First-Order Reversal Curve diagrams.

in oxic environments, and this component was interpreted to be carried by detrital maghemite (Sakuramoto et al., 2017; Yamazaki, 2008, 2009; Yamazaki & Solheid, 2011). The middle-coercivity component of this core is the most dominant component in the IRM decomposition, whereas the proportion of the middle-coercivity component reported previously from the Pacific sediments is smaller than other lower coercivity components in general. This may be caused by a larger input of detrital magnetic minerals due to a close distance of this site from the South American continent.

Low-temperature measurements revealed that samples above ~13 m in depth show blurred Verwey transition, whereas the Verwey transition becomes clearer in the deeper part of the core (Figure 7). This suggests that magnetites in the former samples were partially oxidized to maghemite (Cui et al., 1994; Özdemir et al., 1993). In magnetization curves during a zero-field cooling and warming cycle of an IRM acquired at 300 K, magnetization at temperatures below the Verwey transition temperature (T_v) remains larger than the initial magnetization at 300 K for samples above ~13 m in depth, whereas magnetization becomes smaller than the initial IRM for samples at 13.35 and 16.05 m (Figure 7). The ratio of IRMs at 50–300 K in the cooling curve represents the difference in the shape of the cycling curves mentioned above (Figure 7g), which can be a proxy for oxidation of magnetite (Özdemir & Dunlop, 2010; Yamazaki & Solheid, 2011). These data suggest that surface of magnetites in the sediments above ~13 m in depth has been maghemitized, whereas magnetites in the two samples below ~13 m are little oxidized.

The results of the IRM coercivity analyses and the low-temperature measurements indicate that the sediments above ~13 m in depth have the middle-coercivity component of presumably detrital origin with the mean coercivity of 110–120 mT, and magnetites in these samples suffered from maghemitization. Below ~13 m, the samples in which magnetites are little oxidized and the coercivity of the middle-coercivity component is lower correspond to lows of a^* and b^* in core color (Figures S1 and S3 in Supporting Information S1). These color changes are indicative of a less oxic condition. We interpret the observation that detrital magnetites in the sediments were maghemitized at their surfaces by the time of deposition and then maghemites were reduced to magnetites in a suboxic environment in the deeper part of the core. We infer that loss of maghemite shell by reduction caused a decrease in the mean coercivity; the maghemite shell can have an enhanced coercivity due to stress induced by oxidation (Cui et al., 1994; van Velzen & Zijderveld, 1995). Some authors previously documented magnetic property changes across the iron-redox boundary: decreased coercivity and remanent coercivity of bulk pelagic sediments (Smirnov & Tarduno, 2000) and disappearance of the middle-coercivity component with the mean of ~100 mT (Yamazaki & Ikehara, 2012; Yamazaki & Solheid, 2011).

All FORC diagrams show a narrow ridge along $H_u \approx 0$. This feature is called the central ridge, and its peak coercivity is about 25 mT (Figures 6e–6h; Figures S2k–S2t in Supporting Information S1). The central ridge indicates the presence of non-interacting SD grains, which is interpreted to be carried by intact chains of magnetofossils (Chang et al., 2014; Chen et al., 2007; Egli et al., 2010; Li et al., 2012; Roberts et al., 2012; Yamazaki, 2008). The presence of magnetofossils is supported by the TEM observation (Figure S4 in Supporting Information S1). SD-size particles with typical morphologies observed for magnetosomes produced by magnetotactic bacteria, these are hexagonal prisms, equant octahedra, and tear-drops, were observed. The FORC diagrams also have a broad component with wide H_u distributions, whose coercivity extends to 120 mT or higher. The large vertical (H_u) spread indicates the presence of significant magnetostatic interactions, which is interpreted to be carried by detrital magnetic grains in vortex states and/or aggregated detrital grains with significant inter-grain magnetostatic interactions. Magnetofossils of multi-stranded, bended, and collapsed chains would also contribute to the broad component in a lower coercivity range (Amor et al., 2022; Berndt et al., 2020; Chang et al., 2019). The broad component is small for the sample at 6.06 m in depth, indicating a smaller proportion of the detrital component (Figure 6b). This is consistent with a high in $k_{\text{ARM}}/\text{SIRM}$ at and near the depth of this sample (Figure 5b), suggesting a larger proportion of magnetofossils. In the samples that have the decreased mean coercivity of the middle-coercivity component in the IRM decomposition (13.35 and 16.05 m), the coercivity distribution of the broad component in the FORC diagrams shifts to the lower side of coercivity compared with other samples (Figure 6h; Figure S2r in Supporting Information S1). On the other hand, the central ridge component does not show remarkable change in its coercivity distribution (Figure 6; Figure S2 in Supporting Information S1), which is consistent with almost constant mean coercivity and DP of the low-coercivity component throughout the core in the IRM decomposition. These observations suggest that detrital magnetites were partially oxidized to maghemites at deposition and then reduced to magnetites in a less oxic environment in the deeper part of the core, whereas magnetofossils have remained unoxidized since their production.

Principal component analysis (PCA) was applied to a set of FORC diagrams (Harrison et al., 2018; Lascu et al., 2015). Fifteen samples having measurements up to 140 mT in H_c and above 13 m in depth, where

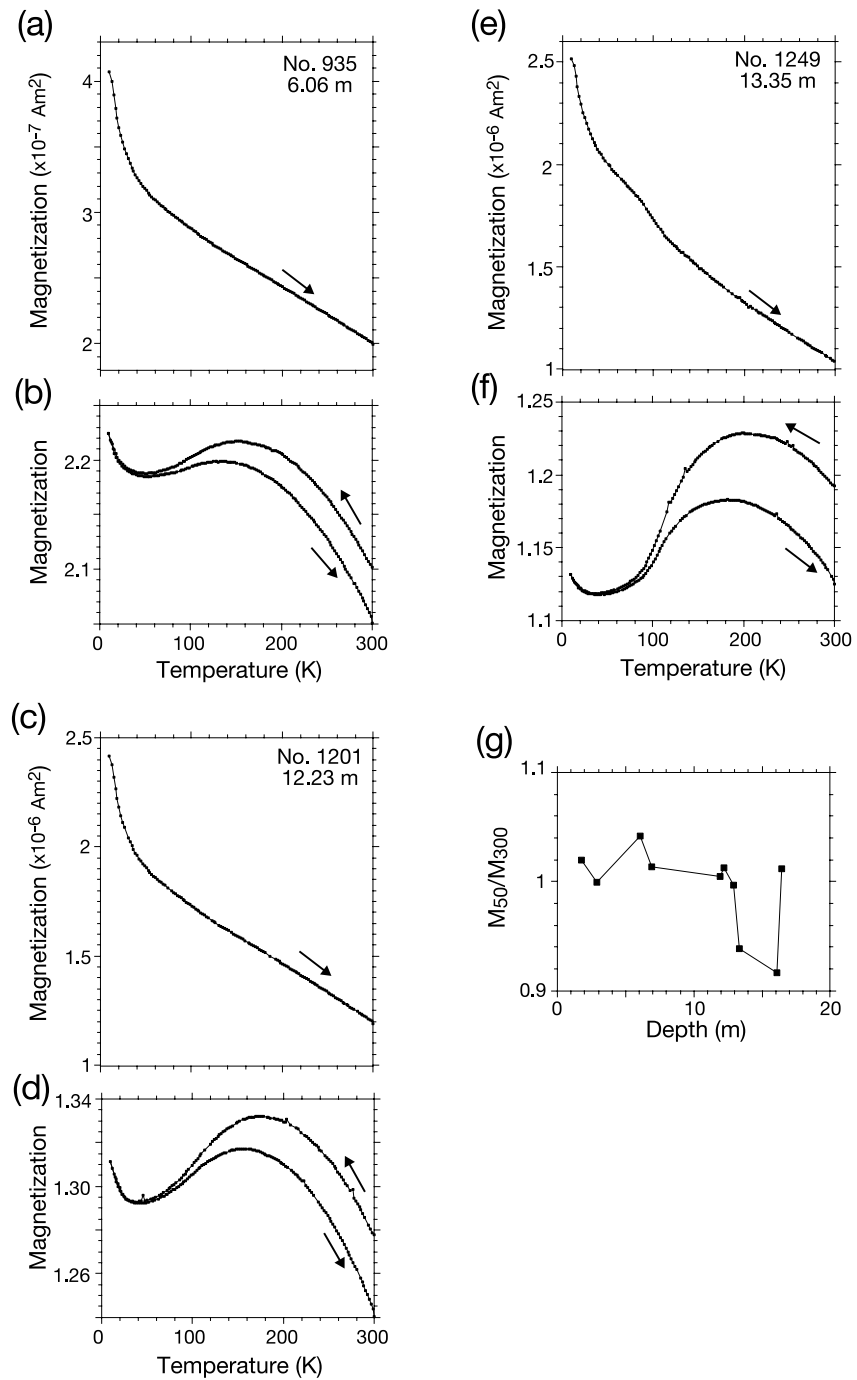


Figure 7. Results of low-temperature magnetic measurements. (a, c, e) Examples of thermal decay of isothermal remanent magnetization (IRM) after cooling from 300 to 10 K in a 3 T field. (b, d, f) Examples of low-temperature cycling of IRM acquired at 300 K in a 3 T field. (g) The ratio of IRMs at 300 and 50 K measured during zero-field cooling of IRM acquired at 300 K.

oxic-redox magnetic mineralogical change does not occur, were selected for the analysis. From FORC-PCA, a two-EM system is defined in a single PC space (Figure 8). Seventy-eight percent of the data variance is explained by the single PC. Incorporating the second PC did not significantly increase the variance explained (Figure S5 in Supporting Information S1). EM1 has a sharp central ridge with a peak H_c of about 25 mT but also some vertical spread. We interpret that EM1 represents intact and collapsed chains of magnetofossils. The vertical spread in EM1 would be caused by flux-closure states of intact multistranded chains and collapsed chains (Amor

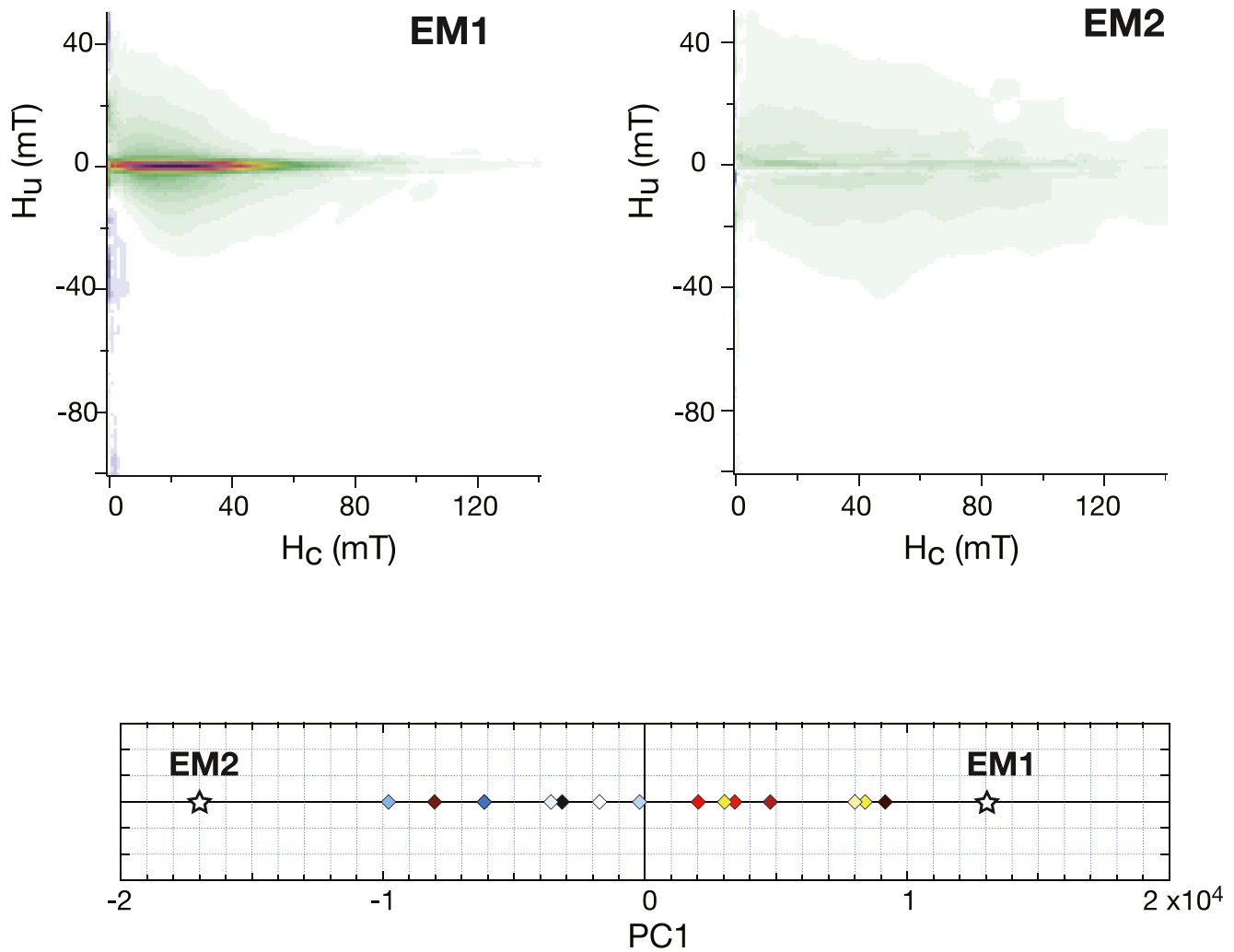


Figure 8. Results of Principal component analysis applied to first-order reversal curve (FORC) diagrams. The lower panel shows distribution of 15 FORC data (diamond) in PC1 space with two-endmembers EM1 and EM2 (star), and the upper panels show FORC diagrams of EM1 and EM2.

et al., 2022). EM2 shows large vertical spread and the FORC distribution extends to ~ 140 mT or higher in H_c , which represents interacting SD/vortex grains of presumably detrital origin. EM1 proportion correlates with $k_{\text{ARM}}/\text{SIRM}$ (Figure 9a), which supports the interpretation that EM1 represents magnetofossils. EM2 proportion correlates with the middle-coercivity component proportion in the IRM decomposition representing partially oxidized detrital magnetites (Figure 9b). In summary, the magnetic mineral assemblage in the sediments above ~ 13 m in depth is a mixture of magnetofossils and partially oxidized detrital magnetites.

From the chemical digestion experiment, the fraction of SIRM carried by silicate-hosted magnetic inclusions is estimated to be about 4% in the average of the three samples (Table 1). Hence most detrital magnetic minerals in the studied sediments are inferred to occur as unprotected grains. Mass-normalized SIRM of silicate-hosted magnetic inclusions in these sediments is $2\text{--}3 \times 10^{-3} \text{Am}^2/\text{kg}$, which is similar to those extracted from sediments of the Ontong-Java Plateau in the western equatorial Pacific (Li et al., 2022) and a little larger than those from red clay in the South Pacific Gyre (Usui et al., 2018).

5. Relative Paleointensity

ARM and IRM are used as the normalizers for RPI estimations in this study, as numerous previous RPI studies did (e.g., Tauxe, 1993; Tauxe & Yamazaki, 2015). We followed the pseudo-Thellier approach (Tauxe et al., 1995), but stepwise demagnetization of ARM and IRM was used instead of acquisition (Channell et al., 2002; Lerner

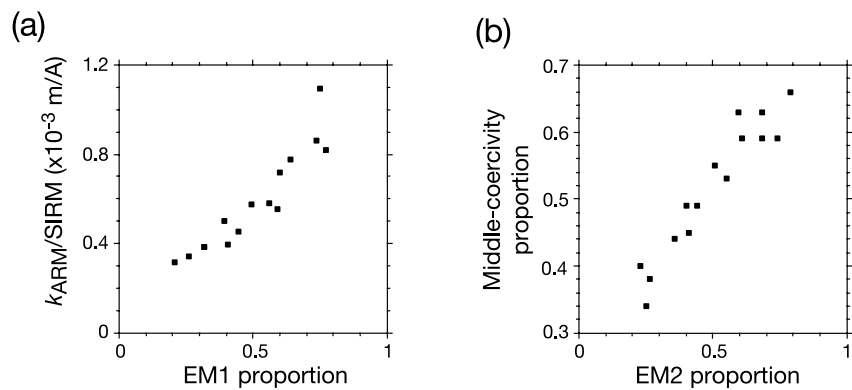


Figure 9. (a) Relation between endmember EM1 proportion from FORC-PCA and the k_{ARM} /saturation isothermal remanent magnetization ratio, and (b) relation between endmember EM2 proportion and middle-coercivity component proportion in isothermal remanent magnetization decomposition.

et al., 2017). Stepwise AF demagnetization of ARM was conducted at the same steps as demagnetizing NRM: 10 steps up to 80 mT for the samples whose NRM was measured with the pass-through cryogenic magnetometer, and 14 steps up to 140 mT and 16 steps up to 160 mT for the samples measured with the discrete cryogenic magnetometer and the spinner magnetometer, respectively. Stepwise demagnetization of IRM was conducted only for the samples in which NRM was AF demagnetized by the tumbling method using the build-in AF demagnetizer of the spinner magnetometer system or the standalone AF demagnetizer, and the same AF steps as demagnetizing NRM were used: 14 steps up to 140 or 16 steps up to 160 mT.

Stepwise AF demagnetizations of NRM ARM, and IRM show different coercivity spectra (Figure S6 in Supporting Information S1), which results in strongly convex diagrams of plotting a pair of NRM and ARM (or IRM) for each AF demagnetization step (Figures 2 and 3). Most ARM was erased by AF demagnetization up to 70 mT not only for the samples to which ARM was imparted at a peak AF of 80 mT but also those to which ARM was imparted at 160 mT. RPI normalized by ARM was calculated from the best-fitting slope in a segment from 20 to 40 mT on NRM-ARM diagrams. Samples with $MAD > 10^\circ$ or slope correlation coefficient < 0.9 (< 0.7 for the samples measured with the spinner magnetometer) were excluded. Variations of RPIs obtained from ARM imparted at 80 mT and that at 140 or 160 mT coincide, but the absolute values are not the same due to the different AF demagnetization efficiency between the static (the former) and tumbling (the latter) AF demagnetization systems; we call $NRM/ARM_{20-40mT_static}$ and $NRM/ARM_{20-40mT_tumbler}$. $NRM/ARM_{20-40mT_static}$ is about 30% larger in average than the other.

Two linear segments are observed in NRM-IRM demagnetization diagrams, from 20 to 40 mT and 70 to 160 mT (Figure 3), and RPI normalized by IRM was calculated separately from the best-fitting slopes in these two segments: $NRM/IRM_{20-40mT}$ and $NRM/IRM_{70-160mT}$. Data with $MAD > 10^\circ$ or slope correlation coefficient < 0.7 were excluded. $NRM/IRM_{70-160mT}$ is significantly larger than $NRM/IRM_{20-40mT}$ as can be recognized from the difference of the slope gradient in Figure 3. The two coercivity ranges, from 20 to 40 mT and from 70 to 160 mT, nearly correspond to those of the low- and middle-coercivity components in the results of the IRM decomposition. Thus, we consider that RPI from $NRM/IRM_{20-40mT}$ is carried by magnetofossils, and RPI from $NRM/IRM_{70-160mT}$ is carried mainly by partially oxidized unprotected magnetites of detrital origin. The observation

Table 1
Summary of Chemical Extraction of Quartz and Feldspar

Sample No.	Depth (m)	Bulk SIRM untreated (10^{-6} Am^2)	Bulk SIRM residues (10^{-6} Am^2)	SIRM fraction residues (%)	Mass fraction residues (%)	Mass-normalized SIRM: untreated ($10^{-3} \text{ Am}^2/\text{kg}$)	Mass-normalized SIRM: untreated ($10^{-3} \text{ Am}^2/\text{kg}$)
755	1.88	30.71	1.30	4.22	22.20	12.88	2.43
935	6.06	9.49	0.48	5.09	8.23	3.94	2.43
1187	11.91	84.77	2.73	3.22	48.11	45.71	3.06

that ARM little carries a coercivity component higher than 70 mT even for ARM acquired at AF of 160 mT supports the interpretation that the middle-coercivity component of the IRM decomposition is mainly of detrital origin and magnetofossils little contribute to this component (Zhang et al., 2022).

The rock magnetic investigation of the core revealed that magnetic mineralogy is uniform down to ~13 m in depth, and that the magnetic mineral assemblage is a mixture of magnetofossils and detrital partially oxidized unprotected magnetites. Below ~13 m, on the other hand, uniformity of magnetic mineralogy, which is a prerequisite of reliable RPI estimations (e.g., Tauxe, 1993; Tauxe & Yamazaki, 2015), is not satisfied; the oxidation state of magnetic minerals changes associated with cyclic oxic-suboxic environmental changes. Thus, the following discussion on RPI is limited to depths above 13 m.

6. Discussion

RPI from this core using NRM-ARM slopes ($\text{NRM}/\text{ARM}_{20-40\text{mT_static}}$) is well correlative to the PISO-1500 stack (Channell et al., 2009) (Figure 10). RPIs from $\text{NRM}/\text{ARM}_{20-40\text{mT_tumbler}}$, $\text{NRM}/\text{IRM}_{20-40\text{mT}}$, and $\text{NRM}/\text{IRM}_{70-160\text{mT}}$ coincide well when scaled to a common average (unity) (Figure 11a). This indicates that all three RPI proxies have preserved the same geomagnetic signals. However, the values of $\text{NRM}/\text{IRM}_{70-160\text{mT}}$ are about 2.3 times larger than those of $\text{NRM}/\text{IRM}_{20-40\text{mT}}$ in average, which indicates that RPI recording efficiency of the detrital component is larger than that of the magnetofossil component when normalized by IRM. This supports the conclusion of Inoue et al. (2021) and Li et al. (2022). It was confirmed by the chemical digestion experiment that the detrital component of Li et al. (2022) and this study consists mainly of unprotected magnetites/maghemites and contribution of silicate-hosted magnetic inclusions is small. There is no discernible phase difference among RPIs from $\text{NRM}/\text{ARM}_{20-40\text{mT_static}}$, $\text{NRM}/\text{IRM}_{20-40\text{mT}}$, and $\text{NRM}/\text{IRM}_{70-160\text{mT}}$, although depth resolution of this study is relatively low due to a relatively large depth interval, ~25 cm, of the samples subjected to demagnetization up to 160 mT. This implies that there is no remarkable difference in DRM fixing depth between the magnetizations carried by the magnetofossil and detrital components. This supports the inference of some previous works that tried to separate remanent magnetization carried by the two components (Gai et al., 2021; Ouyang et al., 2014).

In the studied core, no correlation between RPI and $k_{\text{ARM}}/\text{SIRM}$ is observed (Figures 5 and 10b). There is a gradual upcore decreasing trend in $k_{\text{ARM}}/\text{SIRM}$ above ~13 m in depth, but not in RPI. The degree to which the curves of the PISO-1500 and the RPI of the studied core match does not change with age (Figure 10b) despite $k_{\text{ARM}}/\text{SIRM}$ variations. This is in contrast to the inverse correlation between RPI and $k_{\text{ARM}}/\text{SIRM}$ reported previously (Li et al., 2022; Sakuramoto et al., 2017; Yamazaki et al., 2013). Influence of short-wavelength fluctuation in $k_{\text{ARM}}/\text{SIRM}$ is not observed either. For example, RPI of this core does not show any deviation from the PISO-1500 stack even at a prominent peak in $k_{\text{ARM}}/\text{SIRM}$ at ~6 m in depth (~400 ka) (Figure 10b). In this core, the coercivity ranges of the magnetofossil and detrital components obtained from the IRM decomposition little overlap, and hence RPIs calculated from the two separate coercivity intervals, $\text{NRM}/\text{IRM}_{20-40\text{mT}}$ and $\text{NRM}/\text{IRM}_{70-160\text{mT}}$, could successfully separate RPIs carried by the magnetofossil and detrital components. Therefore, RPI is not influenced even when the proportion of magnetofossils to detrital unprotected magnetite/maghemite changes. In this respect, magnetic properties of this core are ideal for obtaining reliable RPI.

The lower RPI recording efficiency of magnetofossils when normalized by ARM can be partly explained by that higher ARM acquisition efficiency of magnetofossils causes underestimation of RPI (Li et al., 2022; Yamazaki, 2008; Zhang et al., 2022). This study confirmed that lower RPI recording efficiency of magnetofossils occurs also for RPI normalized by IRM, which was previously suggested from calculating RPI separately from different coercivity ranges like this study (Li et al., 2022) or inverse correlation with $k_{\text{ARM}}/\text{SIRM}$ (Inoue et al., 2021; Sakuramoto et al., 2017; Yamazaki et al., 2013). This result suggests that DRM recording efficiency is lower in magnetofossils than detrital unprotected magnetites/maghemites and/or IRM acquisition efficiency may also be influenced by the strength of magnetostatic interactions. The difference in RPI recording efficiency between these two components of this study, about 2.3 times, is significantly larger than that of Li et al. (2022), 1 to 1.5 times. This may be due to that the coercivity ranges of the magnetofossil and detrital components little overlap in this study whereas the two could not be separated completely in Li et al. (2022) because of significantly overlapping coercivity ranges.

It is considered that magnetofossils in sediments occur as a mixture of intact single- and multi-stranded chains and collapsed chains. The configuration of magnetofossils may also influence RPI estimations as well as the proportion of the magnetofossil and detrital components. Although the RPIs from $\text{NRM}/\text{ARM}_{20-40\text{mT_tumbler}}$

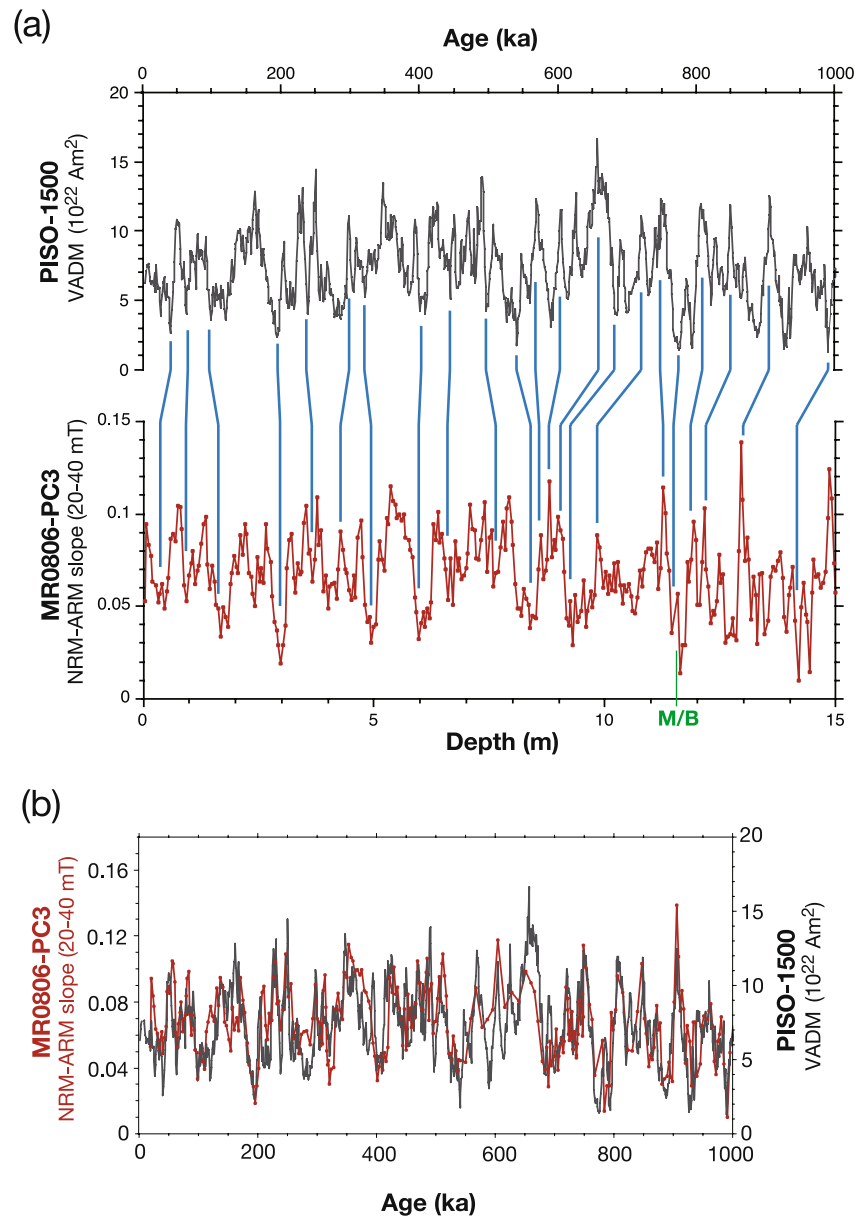


Figure 10. (a) Relative paleointensity (RPI) obtained from Core MR0806-PC3 based on best-fit slopes for a coercivity interval from 20 to 40 mT in NRM-ARM demagnetization diagrams ($\text{NRM}/\text{ARM}_{20-40\text{mT,static}}$), and its correlation to the PISO-1500 RPI stack (Channell et al., 2009). Green line indicates the Matuyama-Brunhes (M/B) boundary based on the directional data shown in Figure 4. (b) Superposition of RPI of Core MR0806-PC3 and the PISO-1500 stack based on the correlation in panel (a).

$\text{NRM}/\text{IRM}_{20-40\text{mT}}$, and $\text{NRM}/\text{IRM}_{70-160\text{mT}}$ coincide in general when the means of the individual RPIs are normalized to unity, there are certain differences among the three (Figure 11a). The difference may be explained by variations in magnetofossil configurations.

In some samples, $\text{NRM}/\text{IRM}_{20-40\text{mT}}$ is larger than the other two, as exemplified by the samples at 5.99 and 7.61 m. In this case, $\text{NRM}/\text{IRM}_{20-40\text{mT}}$ normalized by $\text{NRM}/\text{IRM}_{70-160\text{mT}}$ is positively correlated with $k_{\text{ARM}}/\text{SIRM}$ ($r = 0.64$) (Figure 11b). This may be explained by an increased proportion of magnetofossils forming single stranded chains. In multistranded magnetofossil chains, non-central-ridge low-coercivity contributions in FORC diagrams are associated with a higher-coercivity central-ridge component (Amor et al., 2022), and hence $\text{IRM}_{20-40\text{mT}}$ contains contribution from NRM with a higher coercivity range, which lowers $\text{NRM}/\text{IRM}_{20-40\text{mT}}$. This is not the case for single stranded chains. It is thus expected that $\text{NRM}/\text{IRM}_{20-40\text{mT}}$ enhances with increased

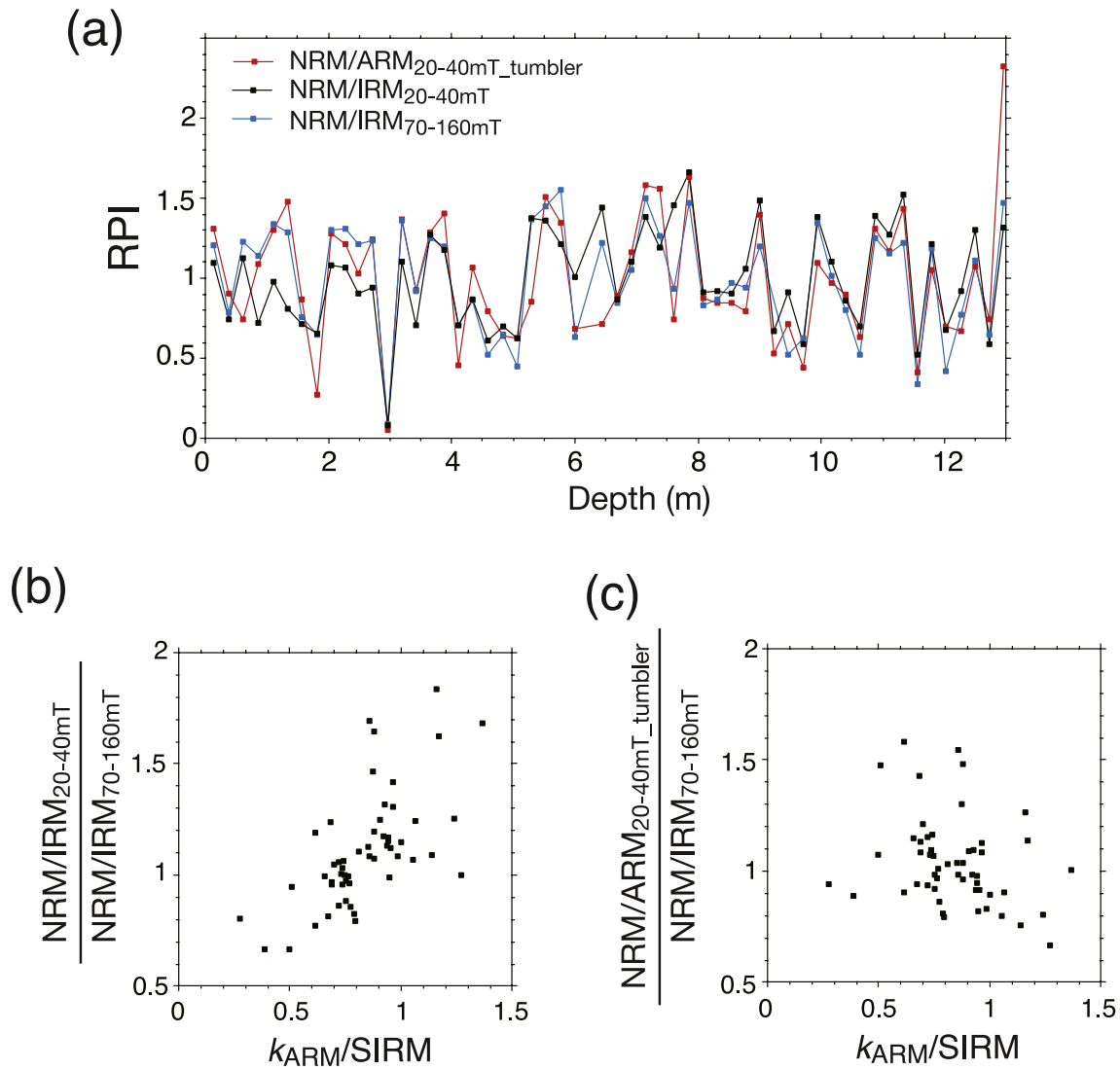


Figure 11. (a) Comparison of RPIs measured on identical samples: NRM-ARM slope from a coercivity interval from 20 to 40 mT (NRM/ARM_{20-40mT_tumbler}) (red), NRM-IRM slope from 20 to 40 mT (NRM/IRM_{20-40mT}) (black), and NRM-IRM slope from 70 to 160 mT (NRM/IRM_{70-160mT}) (blue). All curves are scaled to have a common average (unity). (b) Relation between $k_{ARM}/SIRM$ and NRM/IRM_{20-40mT} normalized by NRM/IRM_{70-160mT}. (c) Relation between $k_{ARM}/SIRM$ and NRM/ARM_{20-40mT_tumbler} normalized by NRM/IRM_{70-160mT}.

proportion of single-stranded chains. Higher ARM acquisition efficiency of single stranded chains compared with multistranded ones enhances $k_{ARM}/SIRM$ ratios.

On the other hand, some samples show larger NRM/ARM_{20-40mT_tumbler} as observed at 4.34, 4.57, and 7.38 m, and have a weak negative correlation with $k_{ARM}/SIRM$ ($r = 0.28$) when NRM/ARM_{20-40mT_tumbler} is normalized by NRM/IRM_{70-160mT} (Figure 11c). This case may be explained by an increased proportion of magnetofossils with intact multistranded chains. ARM acquisition efficiency is lowered in multistranded chains due to magnetostatic interactions among chains, whereas intact multistranded chains have large NRM, which enhances NRM/ARM_{20-40mT_tumbler}. The influence of increased multistranded chains to $k_{ARM}/SIRM$ could be obscured because the ratio can also be lowered by chain collapse. Since NRM/IRM_{20-40mT} and NRM/ARM_{20-40mT_tumbler} could be influenced by changes in magnetofossil configurations as discussed above, we consider that NRM/IRM_{70-160mT} would be the most reliable RPI proxy among the three in the studied core.

This study has demonstrated that for reliable RPI estimations from sediments it is important to evaluate RPI separately for each magnetic mineral constituent in magnetic mineral assemblages. Linearity in NRM-ARM and NRM-IRM demagnetization plots cannot be an indicator for RPI reliability. When coercivity ranges of the magnetofossil and

detrital components completely overlap, NRM-ARM and NRM-IRM demagnetization plots will become linear. Nonetheless, changes in the proportion of the two components will contaminate RPI records, and correlation between RPI and $k_{\text{ARM}}/\text{SIRM}$ will emerge. On the other hand, sediments showing significantly curving NRM-ARM and NRM-IRM demagnetization diagrams like this study have a potential for uncontaminated RPI being recovered owing to little overlapping coercivity ranges of the magnetofossil and detrital components. RPI calculation from a single demagnetization step, which was often conducted before the pseudo-Thellier approach became widely used, should be avoided.

7. Conclusions

We conducted a paleo- and rock magnetic study of a sediment core of about 19 m long taken from the southeast Pacific, which led the following conclusions.

1. The core preserves primary remanent magnetization with little magnetic overprint. The age of the bottom of the core is estimated to be ~ 1.36 Ma from the magnetostratigraphy. A small positive (negative) inclination anomaly is observed during the Brunhes (Matuyama) chron, which is consistent with the time-averaged field models.
2. Magnetofossils and partially oxidized detrital magnetites are main constituents of magnetic mineral assemblages above ~ 13 m in depth. Contribution of silicate-hosted magnetic inclusions to the magnetization is minor. In intercalated suboxic horizons below ~ 13 m, maghemite is reduced to magnetite.
3. Magnetofossils carry magnetization of a coercivity interval from 20 to 40 mT, whereas detrital unprotected magnetites/maghemites carry magnetization of a coercivity interval from 70 to 160 mT for the sediments above ~ 13 m in depth. The detrital component little acquires ARM; ARM imparted at a peak AF of 160 mT was mostly erased after AF demagnetization at 70 mT.
4. The pseudo-Thellier approach was adopted for RPI estimations from the sediments above ~ 13 m. Both NRM-ARM and NRM-IRM demagnetization diagrams show strong convex curvature. RPI calculated from the segment between 20 and 40 mT in NRM-IRM diagrams is lower than that from the segment between 70 and 160 mT. This indicates that RPI recording efficiency of magnetofossils is lower than that of detrital unprotected magnetites/maghemites.
5. IRM-normalized RPI curves from both coercivity segments coincide with the PISO-1500 stack, and they are not influenced by changes in the proportion of magnetofossils to detrital unprotected magnetites/maghemites. This is due to the little overlap in the coercivity distributions of the two components, which is ideal for uncontaminated reliable RPI estimations. However, variations in the configuration of magnetofossils such as intact single- and multi-stranded chains and collapsed chains may still influence RPI estimations.

Data Availability Statement

Paleo- and rock magnetic data produced in this study are available in Zenodo repository at <https://doi.org/10.5281/zenodo.8058086> (Yamazaki et al., 2023). The core material can be requested to the Japan Agency of Marine Earth Science and Technology (JAMSTEC) (https://www.godac.jamstec.go.jp/darwin_tmp/explain/81/e/).

References

- Abe, N. (2009). *MIRAI cruise report MR08-06 Leg1*. Japan Agency for Marine-Earth Science and Technology. <https://doi.org/10.17596/0003282>
- Amor, M., Wan, J., Egli, R., Carlut, J., Gatel, C., Andersen, I. M., et al. (2022). Key signatures of magnetofossils elucidated by mutant magnetotactic bacteria and micromagnetic calculations. *Journal of Geophysical Research: Solid Earth*, 127(1), e2021JB023239. <https://doi.org/10.1029/2021JB023239>
- Banerjee, S. K., King, J., & Marvin, J. (1981). A rapid method for magnetic granulometry with applications to environmental studies. *Geophysical Research Letters*, 8(4), 333–336. <https://doi.org/10.1029/GL008i004p00333>
- Berndt, T. A., Chang, L., & Pei, Z. (2020). Mind the gap: Towards a biogenic magnetite palaeoenvironmental proxy through an extensive finite-element micromagnetic simulation. *Earth and Planetary Science Letters*, 532, 116010. <https://doi.org/10.1016/j.epsl.2019.116010>
- Blatt, H., Jones, R. L., & Charles, R. G. (1982). Separation of quartz and feldspars from mudrocks. *Journal of Sedimentary Research*, 52(2), 660–661. <https://doi.org/10.2110/jsr.52.660>
- Bloemendal, J., King, J. W., Hall, F. R., & Doh, S. J. (1992). Rock magnetism of late Neogene and Pleistocene deep-sea sediments: Relationship to sediment source, diagenetic processes, and sediment lithology. *Journal of Geophysical Research*, 97(B4), 4361–4375. <https://doi.org/10.1029/91JB0306>
- Chang, L., Harrison, R. J., & Berndt, T. A. (2019). Micromagnetic simulation of magnetofossils with realistic size and shape distributions: Linking magnetic proxies with nanoscale observations and implications for magnetofossil identification. *Earth and Planetary Science Letters*, 527, 115790. <https://doi.org/10.1016/j.epsl.2019.115790>
- Chang, L., Hong, H., Bai, F., Wang, S., Pei, Z., Paterson, G. A., et al. (2021). Detrital remanent magnetization of single-crystal silicates with magnetic inclusions: Constraints from deposition experiments. *Geophysical Journal International*, 224(3), 2001–2015. <https://doi.org/10.1093/gji/ggaa559>

Acknowledgments

The core used in this study were obtained by the effort of all personnel related to the *R/V Mirai* MR08-06 cruise Leg 1 (chief scientist: Natue Abe). We also thank Yuhji Yamamoto for supporting paleo- and rock magnetic measurements and providing us his software for the paleomagnetic data analyses, Yoichi Usui and Yusuke Miyairi for the guidance on the chemical digestion experiment, and Nobuhiro Ogawa for the help with TEM observation. The manuscript was significantly improved by insightful review comments from Ramon Egli. Part of this study was performed under the cooperative research program of Marine Core Research Institute, Kochi University (21A006, 21B006, 22A006, 22B005). We acknowledge support from a Grant-in-Aid for Scientific Research (KAKENHI) of the Japan Society for the Promotion of Science (19H01997).

- Chang, L., Roberts, A. P., Heslop, D., Hayashida, A., Li, J., Zhao, X., et al. (2016). Widespread occurrence of silicate-hosted magnetic mineral inclusions in marine sediments and their contribution to paleomagnetic recording. *Journal of Geophysical Research: Solid Earth*, 121(12), 8415–8431. <https://doi.org/10.1002/2016JB013109>
- Chang, L., Roberts, A. P., Winklhofer, M., Heslop, D., Dekkers, M. J., Krijgsman, W., et al. (2014). Magnetic detection and characterization of biogenic magnetic minerals: A comparison of ferromagnetic resonance and first-order reversal curve diagrams. *Journal of Geophysical Research: Solid Earth*, 119(8), 6136–6158. <https://doi.org/10.1002/2014JB011213>
- Channell, J. E. T., Hodell, D. A., Margari, V., Skinner, L. C., Tzedakis, P. C., & Kesler, M. S. (2013). Biogenic magnetite, detrital hematite, and relative paleointensity in Quaternary sediments from the Southwest Iberian Margin. *Earth and Planetary Science Letters*, 376, 99–109. <https://doi.org/10.1016/j.epsl.2013.06.026>
- Channell, J. E. T., Mazaud, A., Sullivan, P., Turner, S., & Raymo, M. E. (2002). Geomagnetic excursions and paleointensities in the Matuyama Chron at Ocean Drilling Program Sites 983 and 984 (Iceland Basin). *Journal of Geophysical Research*, 107(B6), 2114. <https://doi.org/10.1029/2001JB000491>
- Channell, J. E. T., Xuan, C., & Hodell, D. A. (2009). Stacking paleointensity and oxygen isotope data for the last 1.5 Myr (PISO-1500). *Earth and Planetary Science Letters*, 283(1–4), 14–23. <https://doi.org/10.1016/j.epsl.2009.03.012>
- Chen, A. P., Egli, R., & Moskowitz, B. M. (2007). First-order reversal curve (FORC) diagrams of natural and cultured biogenic magnetic particles. *Journal of Geophysical Research*, 112(B8), B08S90. <https://doi.org/10.1029/2006jb004575>
- Chen, L., Heslop, D., Roberts, A. P., Chang, L., Zhao, X., McGregor, H. V., et al. (2017). Remanence acquisition efficiency in biogenic and detrital magnetite and recording of geomagnetic paleointensity. *Geochemistry, Geophysics, Geosystems*, 18(4), 1435–1450. <https://doi.org/10.1002/2016GC006753>
- Clayton, R. N., Rex, R. W., Syers, J. K., & Jackson, M. L. (1972). Oxygen isotope abundance in quartz from Pacific pelagic sediments. *Journal of Geophysical Research*, 77(21), 3907–3915. <https://doi.org/10.1029/JC077i021p03907>
- Cromwell, G., Johnson, C. L., Tauxe, L., Constable, C. G., & Jarboe, N. A. (2018). PSV10: A global data set for 0–10 Ma time-averaged field and paleosecular variation studies. *Geochemistry, Geophysics, Geosystems*, 19(5), 1533–1558. <https://doi.org/10.1002/2017GC007318>
- Cui, Y., Verosub, K. L., & Roberts, A. P. (1994). The effect of low-temperature oxidation on large multi-domain magnetite. *Geophysical Research Letters*, 21(9), 757–760. <https://doi.org/10.1029/94gl00639>
- Egli, R. (2004). Characterization of individual rock magnetic components by analysis of remanence curves.: 2. Fundamental properties of coercivity distributions. *Physics and Chemistry of the Earth*, 29(13–14), 851–867. <https://doi.org/10.1016/j.pce.2004.04.001>
- Egli, R. (2013). VARIFORC: An optimized protocol for calculating non-regular first-order reversal curve (FORC) diagrams. *Global and Planetary Change*, 110, 302–320. <https://doi.org/10.1016/j.gloplacha.2013.08.003>
- Egli, R. (2021). Magnetic characterization of geologic materials with first-order reversal curves. In V. Franco, & B. Dodrill (Eds.), *Magnetic measurement techniques for materials characterization* (pp. 455–604). Springer International Publishing. https://doi.org/10.1007/978-3-030-70443-8_17
- Egli, R., Chen, A. P., Winklhofer, M., Kodama, K. P., & Horng, C.-S. (2010). Detection of noninteracting single domain particles using first-order reversal curve diagrams. *Geochemistry, Geophysics, Geosystems*, 11(1), Q01Z11. <https://doi.org/10.1029/2009GC002916>
- Gai, C., Liu, Y., Shi, X., Sun, C., Jiang, X., Liu, J., et al. (2021). Recording fidelity of relative paleointensity characteristics in the North Pacific Ocean. *Journal of Geophysical Research: Solid Earth*, 126(7), e2021JB022068. <https://doi.org/10.1029/2021JB022068>
- Gradstein, F. M., Ogg, J. G., Schmitz, M. D., & Ogg, G. M. (2020). *Geologic time scale 2020*. Elsevier.
- Harrison, R. J., & Feinberg, J. M. (2008). FORCinel: An improved algorithm for calculating first-order reversal curve distributions using locally weighted regression smoothing. *Geochemistry, Geophysics, Geosystems*, 9(5), Q05016. <https://doi.org/10.1029/2008GC001987>
- Harrison, R. J., Muraszko, J., Heslop, D., Lascu, I., Muxworthy, A. R., & Roberts, A. P. (2018). An improved algorithm for unmixing first-order reversal curve diagrams using principal component analysis. *Geochemistry, Geophysics, Geosystems*, 19(5), 1595–1610. <https://doi.org/10.1029/2018gc007511>
- Heller, F., Lowrie, W., & Channell, J. E. T. (1984). Late Miocene magnetic stratigraphy at Deep Sea Drilling Project Hole 521A. *Initial Reports of the Deep Sea Drilling Project*, 73, 637–644. <https://doi.org/10.2973/dsdp.proc.73.125.1984>
- Hofmann, D. I., & Fabian, K. (2009). Correcting relative paleointensity records for variations in sediment composition: Results from a South Atlantic stratigraphic network. *Earth and Planetary Science Letters*, 284(1–2), 34–43. <https://doi.org/10.1016/j.epsl.2009.03.043>
- Inoue, K., Yamazaki, T., & Usui, Y. (2021). Influence of magnetofossils on paleointensity estimations inferred from principal component analyses of first-order reversal curve diagrams for sediments from the western equatorial Pacific. *Geochemistry, Geophysics, Geosystems*, 22(10), e2021GC010081. <https://doi.org/10.1029/2021GC010081>
- Johnson, C. L., & Constable, C. G. (1997). The time-averaged geomagnetic field: Global and regional biases for 0–5 Ma. *Geophysical Journal International*, 131(3), 643–666. <https://doi.org/10.1111/j.1365-246X.1997.tb06604.x>
- King, J., Banerjee, S. K., Marvin, J., & Özdemir, Ö. (1982). A comparison of different magnetic methods for determining the relative grain size of magnetite in natural materials: Some results from lake sediments. *Earth and Planetary Science Letters*, 59(2), 404–419. [https://doi.org/10.1016/0012-821X\(82\)90142-X](https://doi.org/10.1016/0012-821X(82)90142-X)
- Kirschvink, J. L. (1980). The least-squares line and plane and the analysis of palaeomagnetic data. *Geophysical Journal International*, 62(3), 699–718. <https://doi.org/10.1111/j.1365-246X.1980.tb02601.x>
- Kirschvink, J. L., Kobayashi-Kirschvink, A., & Woodford, B. J. (1992). Magnetite biomineralization in the human brain. *National Academy of Sciences Proceedings of the United States of America*, 89(16), 7683–7687. <https://doi.org/10.1073/pnas.89.16.7683>
- Kopp, R. E., & Kirschvink, J. L. (2008). The identification and biogeochemical interpretation of fossil magnetotactic bacteria. *Earth-Science Reviews*, 86(1–4), 42–61. <https://doi.org/10.1016/j.earscirev.2007.08.001>
- Kruiver, P. P., Dekkers, M. J., & Heslop, D. (2001). Quantification of magnetic coercivity components by the analysis of acquisition curves of isothermal remanent magnetization. *Earth and Planetary Science Letters*, 189(3–4), 269–276. [https://doi.org/10.1016/S0012-821X\(01\)00367-3](https://doi.org/10.1016/S0012-821X(01)00367-3)
- Lascu, I., Harrison, R. J., Li, Y., Muraszko, J. R., Channell, J. E. T., Piotrowski, A. M., & Hodell, D. A. (2015). Magnetic unmixing of first-order reversal curve diagrams using principal component analysis. *Geochemistry, Geophysics, Geosystems*, 16(9), 2900–2915. <https://doi.org/10.1002/2015gc005909>
- Lerner, G. A., Smirnov, A. V., Surovickii, L. V., & Piispa, E. J. (2017). Nonheating methods for absolute paleointensity determination: Comparison and calibration using synthetic and natural magnetite-bearing samples. *Journal of Geophysical Research: Solid Earth*, 122, 1614–1633. <https://doi.org/10.1002/2016JB013777>
- Li, J., Wu, W., Liu, Q., & Pan, Y. (2012). Magnetic anisotropy, magnetostatic interactions and identification of magnetofossils. *Geochemistry, Geophysics, Geosystems*, 13(10), Q10Z51. <https://doi.org/10.1029/2012GC004384>

- Li, J., Yamazaki, T., Usui, Y., Sagawa, T., Kubota, Y., & Kuroda, J. (2022). Understanding the role of biogenic magnetite in geomagnetic paleointensity recording: Insights from Ontong Java Plateau sediments. *Journal of Geophysical Research: Solid Earth*, 127(6), e2022JB024387. <https://doi.org/10.1029/2022JB024387>
- Ohneiser, C., Acton, G., Channell, J. E. T., Wilson, G. S., Yamamoto, Y., & Yamazaki, T. (2013). A middle Miocene relative paleointensity record from the equatorial Pacific. *Earth and Planetary Science Letters*, 374, 227–238. <https://doi.org/10.1016/j.epsl.2013.04.038>
- Opdyke, N. D., Glass, B., Hays, J. D., & Foster, J. (1966). Paleomagnetic study of Antarctic deep-sea cores. *Science*, 154(3747), 349–357. <https://doi.org/10.1126/science.154.3747.349>
- Ouyang, T., Heslop, D., Roberts, A. P., Tian, C., Zhu, Z., Qiu, Y., & Peng, X. (2014). Variable remanence acquisition efficiency in sediments containing biogenic and detrital magnetites: Implications for relative paleointensity signal recording. *Geochemistry, Geophysics, Geosystems*, 15(7), 2780–2796. <https://doi.org/10.1002/2014GC005301>
- Özdemir, Ö., & Dunlop, D. J. (2010). Hallmarks of maghemitization in low-temperature remanence cycling of partially oxidized magnetite nanoparticles. *Journal of Geophysical Research*, 115(B2), B02101. <https://doi.org/10.1029/2009jb006756>
- Özdemir, Ö., Dunlop, D. J., & Moskowitz, B. M. (1993). The effect of oxidation on the Verwey transition in magnetite. *Geophysical Research Letters*, 20(16), 1671–1674. <https://doi.org/10.1029/93gl01483>
- Pike, C. R., Roberts, A. P., & Verosub, K. L. (1999). Characterizing interactions in fine magnetic particle systems using first order reversal curves. *Journal of Applied Physics*, 85(9), 6660–6667. <https://doi.org/10.1063/1.370176>
- Roberts, A. P., Chang, L., Heslop, D., Florindo, F., & Larrasoana, J. C. (2012). Searching for single domain magnetite in the “pseudo-single-domain” sedimentary haystack: Implications of biogenic magnetite preservation for sediment magnetism and relative paleointensity determinations. *Journal of Geophysical Research*, 117(8), B08104. <https://doi.org/10.1029/2012JB009412>
- Roberts, A. P., Heslop, D., Zhao, X., Oda, H., Egli, R., Harrison, R. J., et al. (2022). Unlocking information about fine magnetic particle assemblages from first-order reversal curve diagrams: Recent advances. *Earth-Science Reviews*, 227, 103950. <https://doi.org/10.1016/j.earscirev.2022.103950>
- Roberts, A. P., Heslop, D., Zhao, X., & Pike, C. R. (2014). Understanding fine magnetic particle systems through use of first-order reversal curve diagrams. *Reviews of Geophysics*, 52(4), 557–602. <https://doi.org/10.1002/2014RG000462>
- Roberts, A. P., Pike, C. R., & Verosub, K. L. (2000). First-order reversal curve diagrams: A new tool for characterizing the magnetic properties of natural samples. *Journal of Geophysical Research*, 105(B12), 28461–28475. <https://doi.org/10.1029/2000jb900326>
- Sakuramoto, Y., Yamazaki, T., Kimoto, K., Miyairi, Y., Kuroda, J., Yokoyama, Y., & Matsuzaki, H. (2017). A geomagnetic paleointensity record of 0.6 to 3.2 Ma from sediments in the western equatorial Pacific and remanent magnetization lock-in depth. *Journal of Geophysical Research: Solid Earth*, 122(10), 7525–7543. <https://doi.org/10.1002/2017JB014450>
- Smirnov, A. V., & Tarduno, J. A. (2000). Estimating superparamagnetism in marine sediments with the time dependency of coercivity of remanence. *Journal of Geophysical Research*, 106(B8), 16135–16143. <https://doi.org/10.1029/2001jb000152>
- Stevens, R. L. (1991). Grain-size distribution of quartz and feldspar extracts and implications for flocculation processes. *Geo-Marine Letters*, 11(3), 162–165. <https://doi.org/10.1007/BF02431004>
- Syers, J. K., Chapman, S. L., Jackson, M. L., Rex, R. W., & Clayton, R. N. (1968). Quartz isolation from rocks, sediments and soils for determination of oxygen isotopes composition. *Geochimica et Cosmochimica Acta*, 32(9), 1022–1025. [https://doi.org/10.1016/0016-7037\(68\)90067-7](https://doi.org/10.1016/0016-7037(68)90067-7)
- Tauxe, L. (1993). Sedimentary records of relative paleointensity of the geomagnetic field: Theory and practice. *Reviews of Geophysics*, 31(3), 319–354. <https://doi.org/10.1029/93RG01771>
- Tauxe, L., & Hartl, P. (1997). 11 million years of Oligocene geomagnetic field behavior. *Geophysical Journal International*, 128(1), 217–229. <https://doi.org/10.1111/j.1365-246x.1997.tb04082.x>
- Tauxe, L., Pick, T., & Kok, Y. S. (1995). Relative paleointensity in sediments: A pseudo-Thellier approach. *Geophysical Research Letters*, 22(21), 2885–2888. <https://doi.org/10.1029/95GL03166>
- Tauxe, L., & Yamazaki, T. (2015). Paleointensities. In *Treatise on geophysics* (2nd ed., Vol. 5, pp. 461–509). <https://doi.org/10.1016/B978-0-444-53802-4.00107-X>
- Usui, Y., Shimono, T., & Yamazaki, T. (2018). Rock magnetism of quartz and feldspars chemically separated from pelagic red clay: A new approach to provenance study. *Earth Planets and Space*, 70(1), 153. <https://doi.org/10.1186/s40623-018-0918-1>
- Valet, J.-P., Meynadier, L., & Guyodo, Y. (2005). Geomagnetic dipole strength and reversal rate over the past two million years. *Nature*, 435(7043), 802–805. <https://doi.org/10.1038/nature03674>
- Valet, J.-P., Moreno, E., Bassinot, F., Johannes, L., Dewilde, F., Bastos, T., et al. (2011). Isolating climatic and paleomagnetic imbricated signals in two marine cores using principal component analysis. *Geochemistry, Geophysics, Geosystems*, 12(8), Q08012. <https://doi.org/10.1029/2011GC003697>
- van Velzen, A. J., & Zijdeveld, J. D. A. (1995). Effects of weathering on single-domain magnetite in Early Pliocene marine marls. *Geophysical Journal International*, 121(1), 267–278. <https://doi.org/10.1111/j.1365-246X.1995.tb03526.x>
- Xuan, C., & Channell, J. E. T. (2008). Origin of orbital periods in the sedimentary relative paleointensity records. *Physics of the Earth and Planetary Interiors*, 169(1–4), 140–151. <https://doi.org/10.1016/j.pepi.2008.07.017>
- Yamamoto, Y., Fukami, H., & Lippert, P. C. (2022). Eocene relative paleointensity of the geomagnetic field from Integrated Ocean Drilling Program Site U1403 and U1408 sediments in the northwest Atlantic. *Earth and Planetary Science Letters*, 584, 117158. <https://doi.org/10.1016/j.epsl.2022.117518>
- Yamamoto, Y., Yamazaki, T., Acton, G. D., Richter, C., Guidry, E. P., & Ohneiser, C. (2014). Palaeomagnetic study of IODP Sites U1331 and U1332 in the equatorial Pacific—Extending relative geomagnetic palaeointensity observations through the Oligocene and into the Eocene. *Geophysical Journal International*, 196(2), 694–711. <https://doi.org/10.1093/gji/ggt412>
- Yamazaki, T. (2008). Magnetostatic interactions in deep-sea sediments inferred from first-order reversal curve diagrams: Implications for relative paleointensity normalization. *Geochemistry, Geophysics, Geosystems*, 9(2), Q02005. <https://doi.org/10.1029/2007GC001797>
- Yamazaki, T. (2009). Environmental magnetism of Pleistocene sediments in the North Pacific and Ontong-Java Plateau: Temporal variations of detrital and biogenic components. *Geochemistry, Geophysics, Geosystems*, 10(7), Q07Z04. <https://doi.org/10.1029/2009GC002413>
- Yamazaki, T., & Ikehara, M. (2012). Origin of magnetic mineral concentration variation in the Southern Ocean. *Paleoceanography*, 27(2), PA2206. <https://doi.org/10.1029/2011PA002271>
- Yamazaki, T., & Ioka, N. (1994). Long-term secular variation of the geomagnetic field during the last 200 Kyr recorded in sediment cores from the western equatorial Pacific. *Earth and Planetary Science Letters*, 128(3–4), 527–544. [https://doi.org/10.1016/0012-821x\(94\)90168-6](https://doi.org/10.1016/0012-821x(94)90168-6)
- Yamazaki, T., Li, J., Shimono, T., & Kanamatsu, T. (2023). Rock- and paleomagnetic data of sediment core MR0806-PC3 in the southeast Pacific off Chile [Dataset]. Zenodo <https://doi.org/10.5281/zenodo.8058086>

- Yamazaki, T., & Shimono, T. (2013). Abundant bacterial magnetite occurrence in oxic red clay. *Geology*, *41*(11), 1191–1194. <https://doi.org/10.1130/G34782.1>
- Yamazaki, T., & Solheid, P. (2011). Maghemite-to-magnetite reduction across the Fe-redox boundary in a sediment core from the Ontong-Java Plateau: Influence on relative palaeointensity estimation and environmental magnetic application. *Geophysical Journal International*, *185*(3), 1243–1254. <https://doi.org/10.1111/j.1365-246X.2011.05021.x>
- Yamazaki, T., & Yamamoto, Y. (2018). Relative paleointensity and inclination anomaly over the last 8 Myr obtained from the Integrated Ocean Drilling Program Site U1335 sediments in the eastern equatorial Pacific. *Journal of Geophysical Research: Solid Earth*, *123*(9), 7305–7320. <https://doi.org/10.1029/2018JB016209>
- Yamazaki, T., Yamamoto, Y., Acton, G., Guidry, E. P., & Richter, C. (2013). Rock-magnetic artifacts on long-term relative paleointensity variations in sediments. *Geochemistry, Geophysics, Geosystems*, *14*(1), 29–43. <https://doi.org/10.1002/ggge.20064>
- Zhang, Q., Liu, Q., Li, J., & Sun, Y. (2018). An integrated study of the eolian dust in pelagic sediments from the North Pacific Ocean based on environmental magnetism, transmission electron microscopy, and diffuse reflectance spectroscopy. *Journal of Geophysical Research: Solid Earth*, *123*(5), 3358–3376. <https://doi.org/10.1002/2017JB014951>
- Zhang, Q., Roberts, A. P., Ge, S., Liu, Y., Liu, J., Liu, S., et al. (2022). Interpretation of anhysteretic remanent magnetization carriers in magnetofossil-rich marine sediments. *Journal of Geophysical Research: Solid Earth*, *127*(11), e2022JB024432. <https://doi.org/10.1029/2022JB024432>